Perturbation Observer based Fractional-order Sliding-mode Controller for MPPT of Grid-connected PV Inverters: Design and Real-time Implementation

Bo Yang [1], Tao Yu [2,3,*], Hongchun Shu [1], Dena Zhu [1], Na An [1], Yiyan Sang [4], and Lin Jiang [4]

[1] Faculty of Electric Power Engineering, Kunming University of Science and Technology, 650500 Kunming, China;
[2] College of Electric Power, South China University of Technology, 510640 Guangzhou, China;
[3] Guangdong Key Laboratory of Clean Energy Technology, 510640 Guangzhou, China;
[4] Department of Electrical Engineering & Electronics, University of Liverpool, Liverpool, L69 3GJ, United Kingdom;
* Correspondence: taoyu1@scut.edu.cn, Tel.: +86-130-020-88518

Abstract: In this paper, a robust/adaptive perturbation observer based fractional-order sliding-mode controller (POFO-SMC) is designed for a photovoltaic (PV) inverter connected to the power grid, in which a maximum power point tracking (MPPT) based on variable step size incremental conductance (INC) technique is achieved to harvest the available maximum solar energy from the PV arrays in the presence of various atmospheric conditions. A nonlinear extended state observer (ESO), called sliding-mode state and perturbation observer (SMSPO), is used to efficiently estimate the aggregated effect of PV inverter nonlinearities and parameter uncertainties, unmodelled dynamics, stochastic fluctuation of atmospheric conditions, and external disturbances. Then, a fractional-order sliding-mode controller (FOSMC) is designed to considerably enhance the system robustness via real-time perturbation compensation and to noticeably accelerate the tracking rate compared to the traditional integer-order sliding-mode control (SMC) through employing a fractional-order proportional-derivative (FOPD) sliding surface. In addition, more reasonable control efforts could be realized since the upper bound of perturbation is replaced by its real-time estimate, such that the inherent over-conservativeness of conventional SMC can be effectively reduced. Four case studies are carried out under Matlab/Simulink environment. Simulation results verify the effectiveness and superiority of POFO-SMC compared to that of proportional-integral (PI) control, feedback linearization control (FLC), SMC, robust SMC (RSMC), and FOSMC. Finally, a dSpace based hardware-in-loop (HIL) experiment is undertaken for the purpose of implementation feasibility validation.

Keywords: solar energy; grid-connected PV inverter; MPPT; nonlinear perturbation observer; fractional-order sliding-mode control; HIL experiment

Nomenclature

Variables		*Abbreviations*	
V_{dc}	PV output voltage	**MPPT**	maximum power point tracking
I_{pv}	PV output current	**PV**	photovoltaic
I_{ph}	cell's photocurrent	**LVRT**	low voltage ride-through
I_S	cell's reverse saturation current	**SMSPO**	sliding-mode state and perturbation observer
I_{RS}	cell's reverse saturation current at reference temperature and solar irradiation	**POFO-SMC**	perturbation observer based fractional-order sliding-mode control
T_c	cell's absolute working temperature, K	**SMC**	sliding-mode control
T_{ref}	cell's reference temperature, K	**SVPWM**	space vector pulse width modulation
S	total solar irradiation, W/m^2	**PI**	proportional-integral
E_g	bang-gap energy of the semiconductor used in the cell	**FLC**	feedback linearization control
I_N	output current of the PV array at the Nth sample of time	**SMPO**	sliding-mode perturbation observer
V_{N-1}	output voltage of the PV array at the (N-1)th sample of time	**FOSMC**	fractional-order sliding-mode control
I_{N-1}	output current of the PV array at the (N-1)th sample of time	**AC**	alternating current
α	scaling factor for adjusting the step size of incremental conductance MPPT	**DC**	direct current
$v_{a,b,c}$	three-phase output voltages of the inverter	**MPP**	maximum power point
$e_{a,b,c}$	three-phase voltages of the grid	**FOPD**	fractional-order proportional-derivative
$i_{a,b,c}$	three-phase currents of the grid	**PO**	perturbation observer
$v_{d,q}$	d-q components of the output voltage of the inverter	**HIL**	hardware-in-loop
$e_{d,q}$	d-q components of the grid voltage	**P&O**	perturb and observe
$i_{d,q}$	d-q components of the grid current	**INC**	incremental conductance
ω	AC grid synchronous frequency	**DEM**	distributed energy and microgrids
System parameters		***The control parameters of POFO-SMC***	
q	electron charge, 1.60217733×10^{-19} Cb	λ_{ci}	fractional-order PD$^{\alpha}$ sliding surface gain
A	p-n junction ideality factor, between 1 and 5	α_{ij}	Luenberger observer gains
k	Boltzman's constant, 1.380658×10^{-23} J/K	φ_i, ς_i	fractional-order sliding-mode control gains
k_i	cell's short-circuit current temperature coefficient	ϵ_c	thickness layer boundary of controller
R_s	cell series resistance	ϵ_o	thickness layer boundary of observer
N_p	number of panels connected in parallel	$\alpha1, \alpha2$	operation order
N_s	number of panels connected in series	B_0	constant control gain
V_N	output voltage of the PV array at the Nth sample of time	k_{ij}	sliding surface constants of observer
R_a,R_b,R_c	line resistance of the grid under abc frame	λ_{a1}, λ_{a2}	Luenberger observer roots
L_a,L_b,L_c	line inductance of the grid under abc frame	λ_{k1}, λ_{k2}	sliding surface roots
C	DC bus capacitance	μ	scaling factor for step size adjusting

1. Introduction

The continuous deterioration of the global environment and the severe green house phenomenon are significantly threatening all living creatures on earth, which are mainly caused by the unlimited use of fossil fuels. In order to remedy this issue, distributed energy and microgrids (DEM) are growing rapidly around the modern world in the past decade due to the ever-increasing demand of energy, particularly in the booming economies like China and India, with an ambitious trend of energy efficiency improvement and carbon emission reduction (Liu, Zhang, & Bae, 2017; Yang et al. 2017b, 2018a, 2018b; Liao, Yao, Han, Wen, & Chen, 2017; Liu, Wen, Yao, & Long 2016). In general, deployed DEM usually involves distributed renewables, e.g., wind, solar, biomass, tidal, wave, geothermal, etc.(Yang, Jiang, Wang, Yao, & Wu, 2016), which can provide a promising and effective solution for the emerging energy crisis of both developing and developed countries (Yang, Yu, Shu, Dong, & Jiang, 2018). Among the various renewable energy resources, photovoltaic (PV) system is one of the most common applications thanks to its elegant merits of inexhaustibility of solar energy, pollution free, lack of noises and tear-and-wear without moving parts, ease of assembly and allocation, and relatively low maintenance costs.

Generally speaking, stochastic fluctuation of weather conditions and partial shading conditions are proved to be the most frequent challenges for PV systems, which usually result in a lower power output. Therefore, proper operation of PV system is quite crucial to extract available maximum power under these conditions, which is well-known as the maximum power point tracking (MPPT) (Lai, Mcculloch, & Yan, 2017). Normally, the output voltage corresponding to the maximum output power of PV array significantly varies with both the temperature and solar irradiation (Elobaid, Abdelsalam, & Zakzouk, 2015; Shen, Yao, Wen, & He, 2017). In order to achieve maximum efficiency for PV systems, conventional MPPT algorithms are used such as hill-climbing (Kandemir, Cetin, &

Borekci, 2017), perturb & observe (P&O) (Ahmed & Salam, 2015), incremental conductance (INC) (Al-Dhaifalla, Nassef, Rezk, & Nisar, 2018). These approaches own different levels of simplicity, convergence speed, and hardware implementation.

Thus far, the grid-connected PV systems are attracting enormous attentions over traditional stand-alone PV systems, in which power factor control and reactive power regulation are regarded as the paramount tasks in PV array connection to the power grid. Under such framework, the PV inverter control must achieve desired performance in the sense of fast dynamic response, robustness to disturbances, small tracking error, and low total harmonic distortion Lauria and Coppola (2014). Currently, two types of control strategies have been endeavoured to realize this important goal, e.g., linear control and nonlinear control. For the former one, proportional-integral (PI) control (Dash & Kazerani, 2011; Kadri, Gaubert, & Champenois, 2011), hysteresis (Rahim, Selvaraj, & Krismadinata, 2007), and model predictive controller (Kotsopoulos, Duarte, & Hendrix, 2001) are some typical schemes which have been widely used in PV inverters due to their prominent features of implementation simplicity and high reliability. Basically, they can provide satisfactory control performance over a fixed set of operation points as the original system is linearized at an equilibrium point. However, the PV source usually exhibits a strongly nonlinear electrical behaviour resulted from the stochastic variation of solar irradiation and nonlinear switching functions of inverters, together with the fact that the electrical characteristics of the PV sources are time-varying, hence their control performance may be dramatically degraded over a wide variation in atmospheric conditions.

Alternatively, nonlinear control has also gained plenty of interests in research so as to remedy the aforementioned essential flaws of linear control. References Lalili, Mellit, Lourci, Medjahed and Berkouk (2011); Lalili, Mellit, Lourci, Medjahed and Boubakir (2013) designed a feedback linearization control (FLC) for a two-level and a three-level grid-connected PV inverter, respectively, which fully removes the PV inverter nonlinearities to achieve a globally consistent control performance under various atmospheric conditions. However, an accurate PV system model is required thus it lack of robustness against any system parameter uncertainties or external disturbances. To handle this thorny obstacle, a robust partial feedback linearizing stabilization scheme (Mahmud, Pota, Hossain, & Roy, 2013) was developed for PV inverter, in which the parametric and state-dependent uncertainties are regarded as structured uncertainties, such that all possible modelling uncertainties of nonlinear PV systems can be effectively stabilized. In addition, a model predictive control (MPC) using adaptive multi-context cooperatively coevolving particle swarm optimization (MCCPSO) was proposed to achieve satisfactory performance with respect to overcoming dynamic partial shading, and maximizing the solar energy utilization (Tang, Wu, & Fang, 2017). Furthermore, in work Chiu and Ouyang (2011), T-S fuzzy observer and controller were devised to achieve an asymptotic MPPT for uncertain PV systems, in which the controller and observer gains can be independently solved from linear matrix inequality formulation. Besides, an active disturbance rejection control (ADRC) was employed to provide an efficient dynamic response speed and reduce steady-state errors (Wang, Jin, Zhao, & Yue, 2017).

Among various nonlinear control strategies, sliding-mode control (SMC) is a mature technique which owns elegant features of effective disturbance rejection, fast response, and considerable robustness. Literature Farhat, Barambones and Sbita (2017) adopted SMC associated with the voltage reference estimator and the partial shadow detection unit to achieve MPPT. Moreover, a super twisting algorithm was used to design a second-order SMC for PV system to extract optimal power from solar energy, which can deal with the notorious chattering of the traditional first-order SMC and can even ensure a higher accuracy under imperfect system modelling (Kchaou, Naamane, & Koubaa, 2017). Additionally, a backstepping finite time fast SMC was utilized to avoid the control performance degradation resulted from the uncertainties of PV inverter parameter and system frequency, as well as exogenous inputs (Dhar, & Dash, 2016). However, one inherent weakness of SMC is its over-conservativeness originated from the use of upper bound of uncertainties. In fact, such cases/scenarios does not frequently occur. To tackle this difficult issue, an enormous variety of perturbation observer based SMC (POSMC) schemes have been investigated for numerous engineering problems, such that a proper/reasonable control performance could be realized by a real-time compensation of aggregated uncertainties and external disturbances, e.g., PV pumping systems (Guisser, El-Jouni, & Abdelmounim, 2014), voltage source converter based high voltage direct current (VSC-HVDC) system (Yang et al., 2016), and power systems (Mi et al., 2016).

On the other hand, the aforementioned works operate in the context of integer calculus (IC), i.e., the differentiation and integration are performed in integer order. Fractional calculus (FC) is an extension of regular IC to non-integer scenario. Compared to IC, FC is capable and natural to fully characterize many physical phenomena including viscoelasticity and damping, transmission lines, diffusion, and wave propagation (Atangana, 2016). Basically, the extra freedom degrees of fractional-order integrator and differentiator could further improve the control performance compared with that of conventional integer-order controller. As a consequence, fraction-order SMC (FOSMC) is becoming quite popular in the system control community. Recent applications can be referred to permanent magnet synchronous motor (PMSM) (Zhang, Pi, & Luo, 2012), antilock braking systems (ABS) (Tang, Zhang, Zhang, Zhao, & Guan, 2013), islanded distributed energy resource systems (Delghavi, Shoja-Majidabad, &

Yazdani, 2016), doubly-fed induction generator (DFIG)-based wind turbines (Ebrahimkhani, 2016), etc.

Motivated by the above discussions, this paper attempts to develop a novel SMC scheme through beneficially incorporating the prominent merits of great robustness and reasonable control costs of POSMC and the promising advantages of improved control performance of FOSMC, called perturbation observer based fractional-order SMC (POFO-SMC), for a grid-connected PV inverter to achieve MPPT. The contribution and novelty of this paper can be summarized as follows:

- The PV inverter nonlinearities and parameter uncertainties, unmodelled dynamics, stochastic fluctuation of atmospheric conditions, and external disturbances are aggregated into a perturbation, which is then estimated online by a sliding-mode state and perturbation observer (SMSPO). Hence, the inherent over-conservativeness of SMC can be dramatically reduced;
- The estimated perturbation is completely compensated by an FOSMC associated with a fractional-order PD^{α} sliding surface, such that an improved control performance could be achieved with considerable robustness against to various uncertainties;
- POFO-SMC does not require an accurate PV system model while only the DC link voltage and q-axis current needs to be measured. Moreover, DC link voltage and q-axis current control is fully decoupled;
- Comprehensive case studies are undertaken to evaluate the effectiveness of POFO-SMC and to compare its control performance to that of other typical methods. Moreover, a dSpace based hardware-in-loop (HIL) experiment is carried out to validate the implementation feasibility of the proposed approach.

The rest of this paper is organized as follows: Section 2 devotes to model the grid-connected PV inverter. In Section 3, perturbation observer based fractional-order sliding-mode control is developed. Then, POFO-SMC is applied on PV inverter for MPPT in Section 4. Comprehensive case studies and HIL experiment are presented in Section 5 and Section 6, respectively. In addition, some discussions are given in Section 7. Finally, some concluding marks and future studies are drawn in Section 8.

2. Modelling of Grid-connected PV Inverter

Figure 1 illustrates the schematic configuration of a grid-connected PV inverter, which is consisted of a PV array that transform the solar energy into electricity, a DC link capacitor, a three-phase two-level inverter and a three-phase power grid. In some application, a DC/DC converter will also be included to change the DC voltage into another level, for instance, boost converter, buck converter, and buck-boost converter (Kadri, Gaubert, & Champenois, 2011).

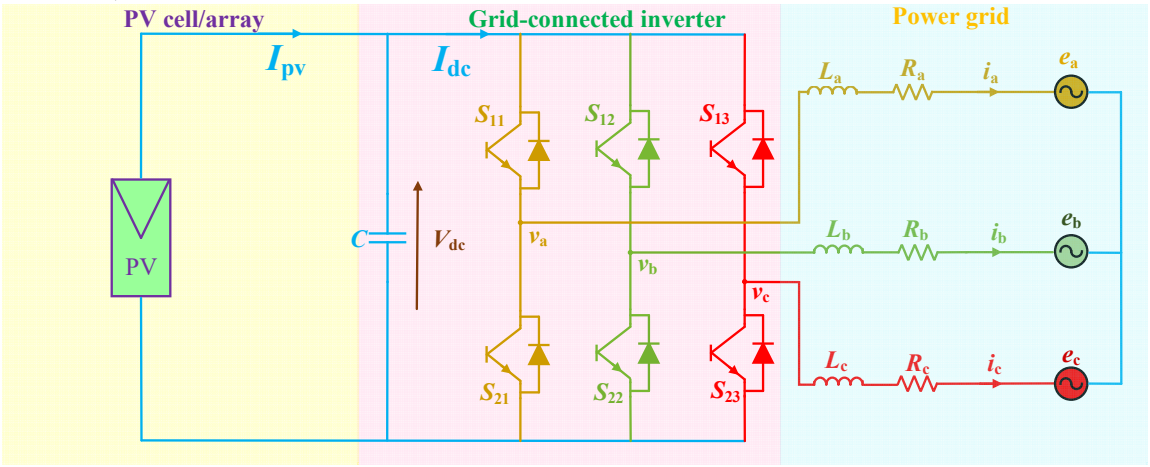

Figure 1. Schematic diagram of a grid-connected PV inverter.

2.1. PV array model

PV cells are usually grouped together in order to form PV modules, which are combined in both series and parallel to provide a desired overall output power (Kotsopoulos, Duarte, & Hendrix, 2001). The following equation describes the relationship between the output current and voltage, as (Lalili, Mellit, Lourci, Medjahed, & Berkouk, 2011; Lalili, Mellit, Lourci, Medjahed, Boubakir, 2013; Yang, et al., 2018c, 2018d)

$$I_{\mathrm{pv}} = N_{\mathrm{p}} I_{\mathrm{ph}} - N_{\mathrm{p}} I_{\mathrm{s}} \left(\exp\left[\frac{q}{AKT_{\mathrm{c}}} \left(\frac{V_{\mathrm{dc}}}{N_{\mathrm{s}}} + \frac{R_{\mathrm{s}} I_{\mathrm{pv}}}{N_{\mathrm{p}}} \right) \right] - 1 \right) \tag{1}$$

where the meaning of each symbol is given in Nomenclature.

The generated photocurrent I_{ph} is calculated as

$$I_{\mathrm{ph}} = \left(I_{\mathrm{sc}} + k_i (T_{\mathrm{c}} - T_{\mathrm{ref}}) \right) \frac{s}{1000} \tag{2}$$

Moreover, the PV cell's saturation current I_{s} is determined by

$$I_{\mathrm{s}} = I_{\mathrm{RS}} \left[\frac{T_{\mathrm{c}}}{T_{\mathrm{ref}}}\right]^3 \exp\left[\frac{qE_{\mathrm{g}}}{Ak}\left(\frac{1}{T_{\mathrm{ref}}} - \frac{1}{T_{\mathrm{c}}}\right)\right] \tag{3}$$

Additionally, the reverse saturation current at the rated temperature and solar irradiation is approximated as

$$I_{\mathrm{s}} = \frac{I_{\mathrm{sc}}}{\exp\left(\frac{qV_{\mathrm{oc}}}{N_{\mathrm{s}}kAT_{\mathrm{c}}}\right) - 1} \tag{4}$$

The above equations (1)-(4) show that the current generated by the PV array is simultaneously relied on the temperature and solar irradiation.

2.2 Three-phase PV inverter model

According to Fig. 1, the dynamics of the PV inverter under the stationary *abc* frame can be described as (Lalili, Mellit, Lourci, Medjahed, & Berkouk, 2011)

$$\begin{cases} v_{\mathrm{a}} = R_{\mathrm{a}} i_{\mathrm{a}} + L_{\mathrm{a}} \frac{\mathrm{d}i_{\mathrm{a}}}{\mathrm{d}t} + e_{\mathrm{a}} \\ v_{\mathrm{b}} = R_{\mathrm{b}} i_{\mathrm{b}} + L_{\mathrm{b}} \frac{\mathrm{d}i_{\mathrm{b}}}{\mathrm{d}t} + e_{\mathrm{b}} \\ v_{\mathrm{c}} = R_{\mathrm{c}} i_{\mathrm{c}} + L_{\mathrm{c}} \frac{\mathrm{d}i_{\mathrm{c}}}{\mathrm{d}t} + e_{\mathrm{c}} \end{cases} \tag{5}$$

After the Park's transformation, the PV inverter dynamics under the synchronous rotating *dq* frame becomes

$$\begin{cases} v_{\mathrm{d}} = e_{\mathrm{d}} + Ri_{\mathrm{d}} + L\frac{\mathrm{d}i_{\mathrm{d}}}{\mathrm{d}t} + \omega L i_{\mathrm{q}} \\ v_{\mathrm{q}} = e_{\mathrm{q}} + Ri_{\mathrm{q}} + L\frac{\mathrm{d}i_{\mathrm{q}}}{\mathrm{d}t} - \omega L i_{\mathrm{d}} \end{cases} \tag{6}$$

where e_{d}, e_{q}, i_{d}, i_{q}, v_{d}, and v_{q} denote the dq-axis components of grid voltage, grid current, and PV inverter output voltage, respectively; *L* and *R* represent the equivalent grid inductance and grid resistance, respectively; and ω means the AC grid synchronous frequency. Furthermore, the power losses of PV inverter switches is ignored, thus one has the following power balance relationship:

$$e_{\mathrm{d}} i_{\mathrm{d}} + e_{\mathrm{q}} i_{\mathrm{q}} = V_{\mathrm{dc}} I_{\mathrm{dc}} \tag{7}$$

where V_{dc} and I_{dc} represent the input voltage and current of the PV inverter, respectively.

At last, the DC link dynamics is given as

$$C\frac{\mathrm{d}V_{\mathrm{dc}}}{\mathrm{d}t} = I_{\mathrm{pv}} - I_{\mathrm{dc}} = I_{\mathrm{pv}} - \frac{e_{\mathrm{d}} i_{\mathrm{d}} + e_{\mathrm{q}} i_{\mathrm{q}}}{V_{\mathrm{dc}}} \tag{8}$$

where C denotes the DC link capacitor.

2.3 Variable step size INC based MPPT

The PV systems should always operate at the maximum output point because of their inherent low efficiency characteristics (Kandemir, Cetin, & Borekci, 2017). Here, Figure 2 provides the diagram of current-voltage (*I-V*) and power-voltage (*P-V*) relationship obtained under various solar irradiation and temperature. It is obvious that a higher temperature will result in a lower MPP while a higher solar irradiation will lead to a higher MPP.

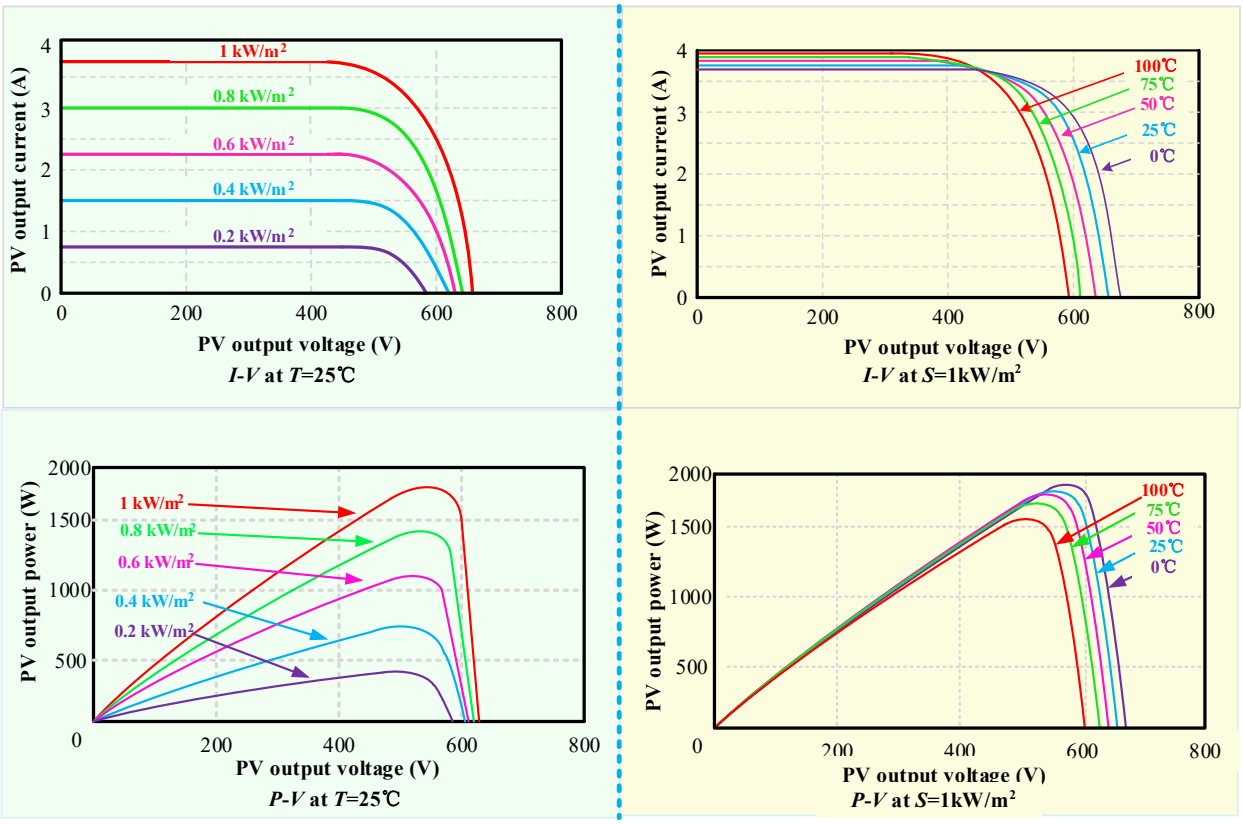

Figure 2. Current-voltage and power-voltage characteristics of PV array obtained under various atmospheric conditions.

Currently, conventional MPPT algorithms are popularly employed thanks to their simplicity. In this paper, INC technique (Kandemir, Cetin, & Borekci, 2017; Al-Dhaifallah, Nassef, Rezk, & Nisar, 2018) is applied to efficiently track the MPP under the rapid time-varying atmospheric conditions, as follows:

$$\begin{cases} \dfrac{\mathrm{d}P}{\mathrm{d}V} = 0, & \text{at MPP} \\ \dfrac{\mathrm{d}P}{\mathrm{d}V} > 0, & \text{left side of MPP} \\ \dfrac{\mathrm{d}P}{\mathrm{d}V} < 0, & \text{right side of MPP} \end{cases} \tag{9}$$

Differentiate the output power $P = VI$ with respect to the output voltage V, it yields

$$\begin{cases} \dfrac{\mathrm{d}P}{\mathrm{d}V} = \dfrac{\mathrm{d}(VI)}{\mathrm{d}V} = I + V\dfrac{\mathrm{d}I}{\mathrm{d}V} \\ \dfrac{\mathrm{d}P}{\mathrm{d}V} = 0 \Longrightarrow \dfrac{\mathrm{d}I}{\mathrm{d}V} \approx \dfrac{\Delta I}{\Delta V} = -\dfrac{I}{V} \end{cases} \tag{10}$$

where $\Delta I/\Delta V$ denotes the incremental conductance and I/V represents the instantaneous conductance, respectively. The MPP can be readily found via comparing I/V to $\Delta I/\Delta V$, by

$$\begin{cases} \dfrac{\Delta I}{\Delta V} = -\dfrac{I}{V}, & \text{at MPP} \\ \dfrac{\Delta I}{\Delta V} > -\dfrac{I}{V}, & \text{left side of MPP} \\ \dfrac{\Delta I}{\Delta V} < -\dfrac{I}{V}, & \text{right side of MPP} \end{cases} \tag{11}$$

The inputs of the MPPT controller are the voltage and current of PV array, while its output is the voltage reference used for space vector pulse width modulation (SVPWM) (Li & Wang, 2009) control of the DC-DC or DC-AC converter connected to the PV array. The variable step size based INC (VSINC) algorithm (Li & Wang, 2009) is adopted in this study, which step size is automatically adjusted according to different operation points, as follows:

$$\varepsilon = \mu \left| \frac{V_N I_N - V_{N-1} I_{N-1}}{V_N - V_{N-1}} \right| \tag{12}$$

where V_N and I_N represent the output voltage and current of the PV array at the Nth iteration; Meanwhile, V_{N-1} and I_{N-1} denote the output voltage and current of the PV array at the (N-1)th iteration; and $\mu = 0.2$ is defined as the scaling factor for online step size adjustment, respectively. Finally, the flowchart of the above algorithm is schematically depicted in Fig. 3.

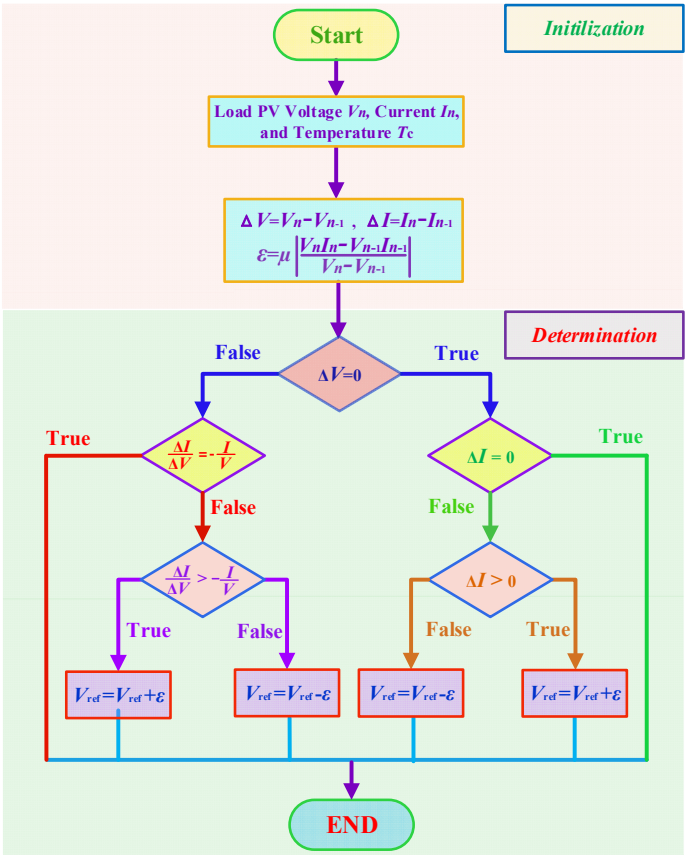

Figure 3. Flowchart of variable step size INC based MPPT algorithm.

Remark 1. It is worth noting that the employed VSINC is only adequate for seeking the global MMP under the uniform solar irradiation condition (single MPP). Basically, these conventional MPPT techniques, e.g., hill-climbing (Kandemir, Cetin, & Borekci, 2017), P&O (Ahmed & Salam, 2015), INC (Al-Dhaifallah, Nassef, Rezk, & Nisar, 2018), may not be able to find the global peak under partial shading condition (PSC) which usually contains multiple local MPPs and one global MPP. In order to overcome this thorny obstacle, soft computing methods (Kandemir, Cetin, & Borekci, 2017) such as fuzzy logic control, artificial neural network, and meta-heuristic algorithms, could be adopted.

3 Perturbation Observer based Fractional-order Sliding-mode Control

3.1 Sliding-mode state and perturbation observer design

Consider an uncertain nonlinear system which has the following canonical form

$$\begin{cases} \dot{x} = Ax + B(a(x) + b(x)u + d(t)) \\ y = x_1 \end{cases} \tag{13}$$

where $x = [x_1, x_2, \cdots, x_n]^{\mathrm{T}} \in \mathcal{R}^n$ represents the state variable vector; $y \in \mathcal{R}$ and $u \in \mathcal{R}$ denote the system output and control input, respectively; $a(x)$: $\mathcal{R}^n \mapsto \mathcal{R}$ and $b(x)$: $\mathcal{R}^n \mapsto \mathcal{R}$ are some unknown smooth functions, which represent the aggregated effect of nonlinearities, parameter uncertainties, and unmodelled dynamics; and $d(t)$: $\mathcal{R}^+ \mapsto \mathcal{R}$ represents a time-varying external disturbance, respectively. The canonical state matrix A and state matrix B are given by

$$A = \begin{bmatrix} 0 & 1 & 0 & \cdots & 0 \\ 0 & 0 & 1 & \cdots & 0 \\ \cdots & \cdots & \cdots & \cdots & \cdots \\ 0 & 0 & 0 & \cdots & 1 \\ 0 & 0 & 0 & \cdots & 0 \end{bmatrix}_{n\times n}, B = \begin{bmatrix} 0 \\ 0 \\ \vdots \\ 0 \\ 1 \end{bmatrix}_{n\times 1} \tag{14}$$

The perturbation of system (13) is defined as (Jiang, Wu, & Wen, 2002)

$$\psi(x, u, t) = a(x) + (b(x) - b_0)u + d(t) \tag{15}$$

where b_0 is a user-defined constant control gain, by which the uncertainties of the control gain $b(x)$ can be aggregated into the perturbation.

For the original system (13), the last state x_n can be rewritten as

$$\dot{x}_n = a(x) + (b(x) - b_0)u + d(t) + b_0 u = \psi(x, u, t) \tag{16}$$

Here, state (16) is consisted of two terms, e.g., perturbation term $\psi(x,u,t)$ that contains all types of uncertainties and control term b_0u which is user-determined.

Now, one can define a *fictitious* state to represent the perturbation, e.g., $x_{n+1}=\psi(x,u,t)$. Then, system (13) can be extended into

$$\begin{cases} y=x_1 \\ \dot{x}_1=x_2 \\ \quad\vdots \\ \dot{x}_n=x_{n+1}+b_0u \\ \dot{x}_{n+1}=\dot{\psi}(\cdot) \end{cases} \tag{17}$$

Therefore, the extended state x_{n+1} is able to separate the unknown perturbation term from the original state x_n.

The new state vector becomes $x_{\mathrm{e}}=[x_1,x_2,\cdots,x_n,x_{n+1}]^{\mathrm{T}}$ for the purpose of simple representation of Eq. (17), and the following three assumptions are made (Yang et al., 2016b, 2017; Jiang, Wu, & Wen, 2002; Dong et al., 2017)

A.1 Constant control gain b_0 must satisfy the following inequality $|\boldsymbol{b(x)/b_0-1}|\leq\boldsymbol{\theta<1}$, where θ is a positive constant.

A.2 The perturbation $\boldsymbol{\psi(x,u,t)}:\boldsymbol{\mathcal{R}^n\times\mathcal{R}\times\mathcal{R}^+\mapsto\mathcal{R}}$ and its first-order derivative $\boldsymbol{\dot{\psi}(x,u,t)}:\boldsymbol{\mathcal{R}^n\times\mathcal{R}\times\mathcal{R}^+\mapsto\mathcal{R}}$ are bounded as $|\boldsymbol{\psi(x,u,t)}|\leq\boldsymbol{\gamma_1}$, $|\boldsymbol{\dot{\psi}(x,u,t)}|\leq\boldsymbol{\gamma_2}$ with $\boldsymbol{\psi(0,0,0)=0}$, and $\boldsymbol{\dot{\psi}(0,0,0)=0}$, where positive constants $\boldsymbol{\gamma_1}$ and $\boldsymbol{\gamma_2}$ are the bounds of perturbation and its first-order derivative, respectively.

A.3 The output reference $\boldsymbol{y_d}$ and its up to *n*th-order derivative are all continuous and bounded.

Throughout this paper, $\tilde{x}=x-\hat{x}$ refers to the estimation error of x whereas $\hat{x}$ represents the estimate of x, while x^* denotes the reference of variable x, respectively. Consider the worst scenario, e.g., $y=x_1$ is the only measurable state, apply an $(n+1)$th-order ESO called SMSPO to simultaneously estimate the states and perturbation of extended system (17), gives (Yang et al., 2016b; Yang et al., 2017; Jiang, Wu, & Wen, 2002)

$$\begin{cases} \dot{\hat{x}}_1=\hat{x}_2+\alpha_1\tilde{x}_1+k_1\mathrm{sat}(\tilde{x}_1,\epsilon_{\mathrm{o}}) \\ \quad\vdots \\ \dot{\hat{x}}_n=\hat{\psi}(\cdot)+\alpha_n\tilde{x}_1+k_n\mathrm{sat}(\tilde{x}_1,\epsilon_{\mathrm{o}})+b_0u \\ \dot{\hat{\psi}}(\cdot)=\alpha_{n+1}\tilde{x}_1+k_{n+1}\mathrm{sat}(\tilde{x}_1,\epsilon_{\mathrm{o}}) \end{cases} \tag{18}$$

where α_i, $i=1,2,\cdots,n+1$, are the Luenberger observer gains which are selected to assign the poles of polynomial $s^{n+1}+\alpha_1s^n+\alpha_2s^{n-1}+\cdots+\alpha_{n+1}=(s+\lambda_\alpha)^{n+1}=0$ to be located in the open left-half complex plane at $-\lambda_\alpha$, with

$$\alpha_i=C_{n+1}^i\lambda_\alpha^i, i=1,2,\cdots,n+1. \tag{19}$$

In addition, positive gains k_i represent the sliding surface constants of the observer, in which

$$k_1\geq|\tilde{x}_2|_{\max} \tag{20}$$

where the ratio k_i/k_1 ($i=2,3,\cdots,n+1$) are chosen to locate the poles of $p^n+(k_2/k_1)p^{n-1}+\cdots+(k_n/k_1)p+(k_{n+1}/k_1)=(p+\lambda_{\mathrm{k}})^n=0$ to be in the open left-half complex plane at $-\lambda_{\mathrm{k}}$, yields

$$\frac{k_{i+1}}{k_1}=C_n^i\lambda_{\mathrm{k}}^i,\ i=1,2,\cdots,n. \tag{21}$$

with $C_n^i=\frac{n!}{i!(n-i)!}$.

Moreover, $\mathrm{sat}(\tilde{x}_1,\epsilon_{\mathrm{o}})$ function (ϵ_{o} denotes the thickness layer boundary of the observer) is employed to replace the conventional $\mathrm{sgn}(\tilde{x}_1)$ function, such that the malignant chattering effect resulted from the discontinuity can be reduced (Yang et al., 2016b).

3.2 Fractional-order sliding-mode controller design

Fractional-order calculus generalizes the integer-order integration and differentiation into the non-integer order domain. The fundamental operator ${}_a\mathrm{D}_t^\alpha$ is defined as (Podlubny, 1999)

$${}_a\mathrm{D}_t^\alpha=\begin{cases}\frac{\mathrm{d}^\alpha}{\mathrm{d}t^\alpha}, & \alpha>0\\ 1, & \alpha=0\\ \int_a^t(\mathrm{d}\tau)^{-\alpha}, & \alpha<0\end{cases} \tag{22}$$

where a and t denote the lower and upper limits while $\alpha\in\mathcal{R}$ means the operation order.

Here, Riemann-Liouville (RL) definition for fractional-order derivative is adopted with *Gamma* function $\Gamma(\cdot)$, as follows

$${}_a\mathrm{D}_t^\alpha f(t)=\frac{1}{\Gamma(n-\alpha)}\frac{\mathrm{d}^n}{\mathrm{d}t^n}\int_a^t\frac{f(\tau)}{(t-\tau)^{\alpha-n+1}}\mathrm{d}\tau \tag{23}$$

where n is the first integer which is not less than α, e.g., $n-1\leq\alpha<n$.

The Laplace transformation of the RL based fractional-order derivative (23) can be obtained as

$$\int_0^\infty{}_0\mathrm{D}_t^\alpha f(t)e^{-st}\mathrm{d}t=s^\alpha\mathcal{L}\{f(t)\}-\sum_{k=0}^{n-1}s^k\,{}_0\mathrm{D}_t^{\alpha-k-1}f(t)|_{t=0} \tag{24}$$

where $\mathcal{L}\{\cdot\}$ represents the Laplace operator.

In addition, the Oustaloup approximation (Yuan, Li, Shao, & Wang, 2016) is used for a recursive distribution of zeros and poles, which gives

$$s^{\alpha} \approx K \prod_{n=-N}^{N} \frac{1+\left(\frac{s}{\omega_{z,n}}\right)}{1+\left(\frac{s}{\omega_{p,n}}\right)}, \quad \alpha > 0 \tag{25}$$

where $2N+1$ denotes the number of zeros and poles; K is the gain which causes both sides of Eq. (25) to have unit gain at 1 rad/s. $\omega_{z,n}$ and $\omega_{p,n}$ are given as

$$\omega_{z,n} = \omega_{\mathrm{b}}\left(\frac{\omega_{\mathrm{h}}}{\omega_{\mathrm{b}}}\right)^{(n+N+(1-\alpha)/2)/(2N+1)} \tag{26}$$

$$\omega_{p,n} = \omega_{\mathrm{b}}\left(\frac{\omega_{\mathrm{h}}}{\omega_{\mathrm{b}}}\right)^{(n+N+(1+\alpha)/2)/(2N+1)} \tag{27}$$

In Eq. (26) and (27), lower limit ω_{b} and upper limit ω_{h} normally satisfy $\omega_{\mathrm{b}}\omega_{\mathrm{h}} = 1$ and $k = \omega_{\mathrm{h}}^{\alpha}$.

The case $\alpha < 0$ can be resolved by inverting Eq. (25). Besides, For $|\alpha| > 1$, the approximation becomes unsatisfactory. In order to handle such case, the fractional powers of s is usually split, as follows

$$s^{\alpha} = s^{n}s^{\delta}, \quad \alpha = n + \delta, \quad n \in \mathcal{Z}, \quad \delta \in [0,1] \tag{28}$$

Hence, only the latter term δ needs to be approximated.

The following Lemma 1 states the stability of fractional-order system.

Lemma 1(Matignon, 1998). Consider the following autonomous system:

$${}_{0}\mathrm{D}_{t}^{\alpha} z = Cz, \qquad z(0) = z_0 \tag{29}$$

where $z \in \mathcal{R}^{n}$ and $C \in \mathcal{R}^{n\times n}$ are asymptotically stable if $|\arg(\mathrm{eig}(C))| > \alpha\pi/2$, in which each component of the states decays towards 0 like $t^{-\alpha}$. Moreover, system (29) is stable if $|\arg(\mathrm{eig}(C))| \geq \alpha\pi/2$ with those critical eigenvalues satisfying $|\arg(\mathrm{eig}(C))| = \alpha\pi/2$ have geometric multiplicity one.

Besides, Figure 4 briefly shows the stability region when $0 < \alpha < 2$. It demonstrates that the stability region of fractional-order system with $0 < \alpha < 1$ is the largest than that of the other two scenarios.

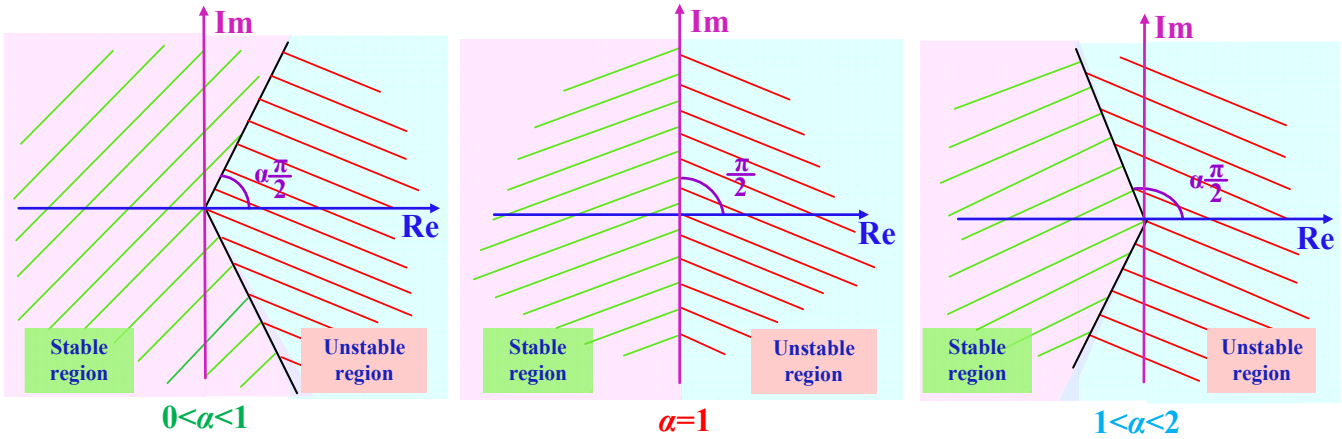

Figure 4. Stability region of fractional-order system determined with varying operation order.

The estimated fractional-order PD^{α} sliding surface for system (13) can be defined as

$$\hat{S}_{\mathrm{FO}} = \Sigma_{i=1}^{n}\left[\rho_i\left(\hat{x}_i - y_{\mathrm{d}}^{(i-1)}\right) + \mathrm{D}^{\alpha}\left(\hat{x}_i - y_{\mathrm{d}}^{(i-1)}\right)\right] \tag{30}$$

where positive constant λ_{c} denotes the fractional-order PD^{α} sliding surface gain.

Let $\hat{S}_{\mathrm{FO}} = 0$, it yields

$$\mathrm{D}^{\alpha}\left(\hat{x}_i - y_{\mathrm{d}}^{(i-1)}\right) = -\rho_i\left(\hat{x}_i - y_{\mathrm{d}}^{(i-1)}\right) \tag{31}$$

According to Lemma 1, one has $C = -\rho_i$ and $|\arg(\mathrm{eig}(C))| = \pi$. When $0 < \alpha < 2$, $|\arg(\mathrm{eig}(C))| > \alpha\pi/2$ can be constantly established. Thus, the dynamics of fractional-order PD^{α} sliding surface (30) is asymptotically stable.

3.3 Overall POFO-SMC design

To this end, the POFO-SMC for system (13) is designed as

$$u = \frac{1}{b_0}[y_{\mathrm{d}}^{(n)} - \hat{\psi}(\cdot) - \varsigma\hat{S}_{\mathrm{FO}} - \varphi\mathrm{sat}(\hat{S}_{\mathrm{FO}}, \epsilon_{\mathrm{c}})] \tag{32}$$

Where sliding-mode control gains ς and φ are chosen to ensure the attractiveness of the estimated fractional-order PD^{α} sliding surface $\hat{S}_{\mathrm{FO}}$. Besides, ϵ_{c} is the thickness layer boundary of controller, function $\mathrm{sat}(\hat{S}_{\mathrm{FO}}, \epsilon_{\mathrm{c}})$ is introduced to replace $\mathrm{sgn}(\hat{S}_{\mathrm{FO}}, \epsilon_{\mathrm{c}})$ for the purpose of chattering reduction of the controller.

4 POFO-SMC Design of PV Inverter

For PV system (1)-(8), define the state vector as $x = (x_1, x_2, x_3)^{\mathrm{T}} = \left(i_{\mathrm{d}}, i_{\mathrm{q}}, V_{\mathrm{dc}}\right)^{\mathrm{T}}$, system output $y = (y_1, y_2)^{\mathrm{T}} = \left(i_{\mathrm{q}}, V_{\mathrm{dc}}\right)^{\mathrm{T}}$, and control input $u = (u_1, u_2)^{\mathrm{T}} = \left(v_{\mathrm{d}}, v_{\mathrm{q}}\right)^{\mathrm{T}}$, respectively. Then, one can obtain the state equation of PV inverter (6) and (8), as follows

$$\dot{x} = f(x) + g(x)u \tag{33}$$

where

$$f(x) = \begin{pmatrix} f_1 \\ f_2 \\ f_3 \end{pmatrix} = \begin{pmatrix} -\frac{R}{L}x_1 - \omega x_2 - \frac{e_{\mathrm{d}}}{L} \\ -\frac{R}{L}x_2 + \omega x_1 - \frac{e_{\mathrm{q}}}{L} \\ \frac{I_{\mathrm{pv}}}{C} - \frac{e_{\mathrm{d}}x_1 + e_{\mathrm{q}}x_2}{Cx_3} \end{pmatrix}; \qquad g(x) = \begin{pmatrix} \frac{1}{L} & 0 \\ 0 & \frac{1}{L} \\ 0 & 0 \end{pmatrix} \tag{34}$$

Now, differentiate the output y until the control input u is explicitly appeared, yields

$$\begin{cases} \dot{y}_1 = -\frac{R}{L}i_{\mathrm{q}} + \omega i_{\mathrm{d}} - \frac{e_{\mathrm{q}}}{L} + \frac{u_2}{L} \\ \ddot{y}_2 = \frac{\dot{I}_{\mathrm{pv}}}{C} - \frac{e_{\mathrm{d}}\left(-\frac{R}{L}i_{\mathrm{d}} - \omega i_{\mathrm{q}} - \frac{e_{\mathrm{d}}}{L}\right) + e_{\mathrm{q}}\left(-\frac{R}{L}i_{\mathrm{q}} + \omega i_{\mathrm{d}} - \frac{e_{\mathrm{q}}}{L}\right)}{CV_{\mathrm{dc}}} - \frac{(e_{\mathrm{d}}i_{\mathrm{d}} + e_{\mathrm{q}}i_{\mathrm{q}})}{C^2V_{\mathrm{dc}}^2}I_{\mathrm{pv}} + \frac{(e_{\mathrm{d}}i_{\mathrm{d}} + e_{\mathrm{q}}i_{\mathrm{q}})^2}{C^2V_{\mathrm{dc}}^3} - \frac{e_{\mathrm{d}}}{LCV_{\mathrm{dc}}}u_1 - \frac{e_{\mathrm{q}}}{LCV_{\mathrm{dc}}}u_2 \end{cases} \tag{35}$$

Then, system (35) can be rewritten into the following matrix form

$$\begin{bmatrix} \dot{y}_1 \\ \ddot{y}_2 \end{bmatrix} = \begin{bmatrix} h_1(x) \\ h_2(x) \end{bmatrix} + B(x)\begin{bmatrix} u_1 \\ u_2 \end{bmatrix} \tag{36}$$

where

$$h_1(x) = -\frac{R}{L}i_{\mathrm{q}} + \omega i_{\mathrm{d}} - \frac{e_{\mathrm{q}}}{L} \tag{37}$$

$$h_2(x) = \frac{\dot{I}_{\mathrm{pv}}}{C} - \frac{e_{\mathrm{d}}\left(-\frac{R}{L}i_{\mathrm{d}} - \omega i_{\mathrm{q}} - \frac{e_{\mathrm{d}}}{L}\right) + e_{\mathrm{q}}\left(-\frac{R}{L}i_{\mathrm{q}} + \omega i_{\mathrm{d}} - \frac{e_{\mathrm{q}}}{L}\right)}{CV_{\mathrm{dc}}} - \frac{(e_{\mathrm{d}}i_{\mathrm{d}} + e_{\mathrm{q}}i_{\mathrm{q}})}{C^2V_{\mathrm{dc}}^2}I_{\mathrm{pv}} + \frac{(e_{\mathrm{d}}i_{\mathrm{d}} + e_{\mathrm{q}}i_{\mathrm{q}})^2}{C^2V_{\mathrm{dc}}^3} \tag{38}$$

with

$$B(x) = \begin{bmatrix} 0 & \frac{1}{L} \\ -\frac{e_{\mathrm{d}}}{LCV_{\mathrm{dc}}} & -\frac{e_{\mathrm{q}}}{LCV_{\mathrm{dc}}} \end{bmatrix} \tag{39}$$

The inverse of control gain matrix $B(x)$ is calculated by

$$B^{-1}(x) = \begin{bmatrix} -\frac{Le_{\mathrm{q}}}{e_{\mathrm{d}}} & -\frac{LCV_{\mathrm{dc}}}{e_{\mathrm{d}}} \\ L & 0 \end{bmatrix} \tag{40}$$

In order to ensure the above input-output linearization to be valid, the control gain matrix $B(x)$ must be nonsingular among the whole operation range, which means

$$\det[B(x)] = \frac{e_{\mathrm{d}}}{L^2CV_{\mathrm{dc}}} \neq 0 \tag{41}$$

Since the d-axis component of the grid voltage e_{d} is always different from zero, the above condition can be always satisfied. Here, functions $h_1(x)$, $h_2(x)$ and matrix $B(x)$ represent the combinatorial effect of the PV inverter nonlinearities and parameter uncertainties, as well as uncertain atmospheric conditions. In practice, their accurate values are difficult to obtain thus need to be estimated by SMSPO.

Define the perturbations $\psi_1(\cdot)$ and $\psi_2(\cdot)$ for PV system (35), as follows:

$$\begin{bmatrix} \psi_1(\cdot) \\ \psi_2(\cdot) \end{bmatrix} = \begin{bmatrix} h_1(x) \\ h_2(x) \end{bmatrix} + (B(x) - B_0)\begin{bmatrix} u_1 \\ u_2 \end{bmatrix} \tag{42}$$

with the constant control gain matrix B_0 being given by

$$B_0 = \begin{bmatrix} b_{11} & 0 \\ 0 & b_{22} \end{bmatrix} \tag{43}$$

where b_{11} and b_{22} are the constant control gains. The diagonal form of matrix B_0 fully decouples the control of q-axis current and DC link voltage. It is worth noticing that such from of matrix B_0 also decouples the observer design of q-axis current and DC link voltage.

The tracking error is now defined as $e = [e_1,\ e_2]^{\mathrm{T}} = [i_{\mathrm{q}}\text{-}i_{\mathrm{q}}^*,\ V_{\mathrm{dc}}\text{-}V_{\mathrm{dc}}^*]^{\mathrm{T}}$, where q-axis current reference i_{q}^* is generally given by the power grid operator while DC link voltage reference V_{dc}^* is determined by VSINC based MPPT technique shown in Fig. 3. Differentiate the tracking error e until the control input u is appeared explicitly, which yields

$$\begin{bmatrix} \dot{e}_1 \\ \ddot{e}_2 \end{bmatrix} = \begin{bmatrix} \psi_1(\cdot) \\ \psi_2(\cdot) \end{bmatrix} + B_0\begin{bmatrix} u_1 \\ u_2 \end{bmatrix} - \begin{bmatrix} \dot{i}_{\mathrm{q}}^* \\ \ddot{V}_{\mathrm{dc}}^* \end{bmatrix} \tag{44}$$

A second-order sliding-mode perturbation observer (SMPO) is adopted to estimate the perturbation $\psi_1(\cdot)$ as

$$\begin{cases} \dot{\hat{i}}_{\mathrm{q}} = \hat{\psi}_1(\cdot) + \alpha_{11}\tilde{i}_{\mathrm{q}} + k_{11}\mathrm{sat}(\tilde{i}_{\mathrm{q}}, \epsilon_{\mathrm{o}}) + b_{11}u_1 \\ \dot{\hat{\psi}}_1(\cdot) = \alpha_{12}\tilde{i}_{\mathrm{q}} + k_{12}\mathrm{sat}(\tilde{i}_{\mathrm{q}}, \epsilon_{\mathrm{o}}) \end{cases} \tag{45}$$

where observer gains k_{11}, k_{12}, α_{11}, and α_{12}, are all positive constants.

Meanwhile, a third-order SMSPO is applied to estimate the perturbation $\psi_2(\cdot)$ as

$$\begin{cases} \dot{\hat{V}}_{\mathrm{dc}} = \hat{V}_{\mathrm{dc}} + \alpha_{21}\tilde{V}_{\mathrm{dc}} + k_{21}\mathrm{sat}(\tilde{V}_{\mathrm{dc}}, \epsilon_{\mathrm{o}}) \\ \dot{\hat{V}}_{\mathrm{dc}} = \hat{\psi}_2(\cdot) + \alpha_{22}\tilde{V}_{\mathrm{dc}} + k_{22}\mathrm{sat}(\tilde{V}_{\mathrm{dc}}, \epsilon_{\mathrm{o}}) + b_{22}u_2 \\ \dot{\hat{\psi}}_2(\cdot) = \alpha_{23}\tilde{V}_{\mathrm{dc}} + k_{23}\mathrm{sat}(\tilde{V}_{\mathrm{dc}}, \epsilon_{\mathrm{o}}) \end{cases} \tag{46}$$

where observer gains k_{21}, k_{22}, k_{23}, α_{21}, α_{22}, and α_{23}, are all positive constants.

The fractional-order PD$^{\alpha}$ sliding surface of tracking error dynamics (44) is chosen as

$$\begin{bmatrix} \hat{S}_{\mathrm{FO1}} \\ \hat{S}_{\mathrm{FO2}} \end{bmatrix} = \begin{bmatrix} \mathrm{D}^{\alpha 1}(\hat{i}_{\mathrm{q}} - i_{\mathrm{q}}^*) + \lambda_{\mathrm{c1}}(\hat{i}_{\mathrm{q}} - i_{\mathrm{q}}^*) \\ \mathrm{D}^{\alpha 2}(\hat{V}_{\mathrm{dc}} - V_{\mathrm{dc}}^*) + \lambda_{\mathrm{c2}}(\hat{V}_{\mathrm{dc}} - V_{\mathrm{dc}}^*) \end{bmatrix} \tag{47}$$

where $\alpha 1$ and $\alpha 2$ are the operation orders, while positive constants λ_{c1} and λ_{c2} denote the fractional-order PD$^{\alpha}$ sliding surface gains, respectively.

Finally, the POFO-SMC design for PV system (35) can be written as

$$\begin{bmatrix} u_1 \\ u_2 \end{bmatrix} = B_0^{-1} \begin{bmatrix} i_{\mathrm{q}}^* - \hat{\psi}_1(\cdot) - \varsigma_1 \hat{S}_{\mathrm{FO1}} - \varphi_1 \mathrm{sat}(\hat{S}_{\mathrm{FO1}}, \epsilon_{\mathrm{c}}) \\ \ddot{V}_{\mathrm{dc}}^* - \hat{\psi}_2(\cdot) - \varsigma_2 \hat{S}_{\mathrm{FO2}} - \varphi_2 \mathrm{sat}(\hat{S}_{\mathrm{FO2}}, \epsilon_{\mathrm{c}}) \end{bmatrix} \tag{48}$$

where positive sliding-mode control gains ς_1, ς_2, φ_1, and φ_2 are chosen to ensure the convergence of tracking error dynamics (44).

Remark 2. It is worth noting that PV system parameters are all aggregated into perturbations (42), which are then estimated by SMPO (45) and SMSPO (46) in the real-time and fully compensated by controller (48). As a result, the change of system parameters will vary the controller output. More specifically, a larger resistance R will result in a smaller controller output u_1 while a larger inductance L will lead to a larger controller output u_1; Meanwhile, a larger resistance R will result in a larger controller output u_2 while a larger inductance L will lead to a smaller controller output u_2. Moreover, the effect of the variation of capacitor C on the controller output u_2 is determined by the relationship of each term in Eq. (38), which depends on the operation points. Lastly, the range of system time parameters is determined by the practical manufacturing standard (normally 50% to 200% of the system parameters tabulated by Table 1), which can be efficiently estimated by SMSPO and compensated by POFO-SMC, such that a satisfactory control performance can be maintained.

For the adopted MPPT algorithm, e.g., VSINC algorithm (Li & Wang, 2009), the stopping criteria of iteration is given as follows:

$$|V_N I_N - V_{N-1} I_{N-1}| \le \mu \tag{49}$$

where the tolerance value μ=0.01W. In other words, the MPPT algorithm will cease once the difference of two consecutive power is smaller than μ.

Note that the conventional linear PID control scheme employs an inner current loop to regulate the current (Kadri, Gaubert, & Champenois, 2011). In contrast, the proposed POFO-SMC (45)-(48) contains no inverter current in its control framework (Yang, Jiang, Yu, Shu, Zhang, Yao, & Wu, 2018e). If an overcurrent of PV inverter occurs resulted from severe faults or malfunctioning of VSC, the installed overcurrent protection devices, such as those published in (Abdel-Salam, Kamel, Khalaf, & Sayed, 2015; Delghavi, Shoja-Majidabad, & Yazdani, 2016) shown in Fig. 5, of PV inverter will be activated to prevent the disturbed PV system from potential damage.

Lastly, the overall control structure of POFO-SMC (45)-(48) for PV system (35) to achieve MPPT is illustrated by Fig. 5. Here, only the q-axis current i_{q} and DC link voltage V_{dc} need to be measured, which are actually transformed from abc framework to dq framework by the use of standard abd/dq transformation module. When the final controller outputs are obtained, e.g., v_{d} and v_{q}, they will be transformed from dq framework to abc framework by the use of standard dq/abc transformation module. Note that the switching frequency of the insulated gate bipolar transistor (IGBT) is decreased by the use of saturation function due to its reduction of frequency and magnitude of the controller output.

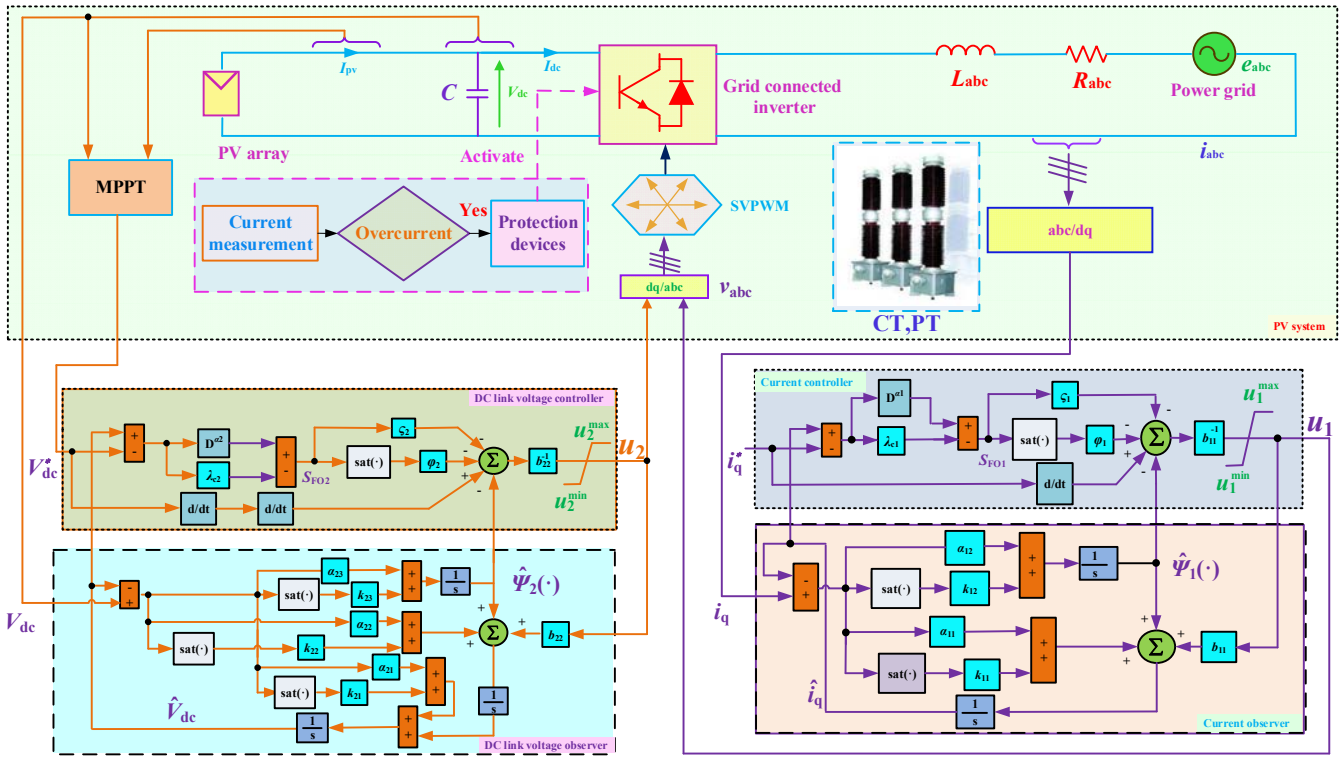

Figure 5. The overall POFO-SMC structure of the grid connected PV inverter for MPPT.

5. Case Studies

The proposed POFO-SMC is applied on a grid connected PV inverter to achieve MPPT under various atmospheric conditions, whose control performance is compared to that of PI control (Kadri, Gaubert, & Champenois, 2011), FLC (Lalili, Mellit, Lourci, Medjahed, & Berkouk, 2011), SMC (Kchaou, Naamane, Koubaa, & M'sirdi, 2017), robust SMC (RSMC) (Mojallizadeh, Badamchizadeh, Khanmohammadi, & Sabahi, 2016), and FOSMC (Zhang, Pi, & Luo, 2012). In addition, Table 1 provides the PV system parameters that are taken directly from reference Lalili, Mellit, Lourci, Medjahed and Berkouk (2011), while POFO-SMC parameters are tabulated in Table 2. Furthermore, the initial solar irradiation and temperature are chosen to be the rated values, e.g., 1 kW/m^2 and 25 ℃, respectively. Moreover, q-axis current is regulated at 0 for a unit power factor (Lalili, Mellit, Lourci, Medjahed, & Berkouk, 2011). The simulation is undertaken using Matlab/Simulink 2016a version with a fixed step size of 10^{-5} and solver ode 4 (Runge-Kutta).

Remark 3. In general, larger observer roots usually result in a higher estimation speed but also leads to a larger estimation error, vice versa. Normally, in order to realize a satisfactory perturbation estimation of the majority of first-order and second-order system, an observer root ranges between 10 to 50 is preferable and sufficient (Yang et al., 2016; Dong et al. 2017). Based on the above analysis, through trial-and-error, observer roots of SMSPO and SMPO are selected as $\lambda_{\alpha 1}$=20 and $\lambda_{\alpha 2}$=10, together with the sliding surface roots λ_{k1}=20 and λ_{k2}=10, respectively, such that a proper trade-off between the estimation speed and estimation error can be achieved. In the case of high-order system, normally the estimation speed has to be compromised thus the estimation error will be considered in priority, hence a relatively small observer root would be used, normally between 5 to 15. Otherwise, significant oscillation and high computational costs will be produced.

Table 1. The PV system parameters (Lalili, Mellit, Lourci, Medjahed, & Berkouk, 2011)

Typical peak power	60W	**Factor of PV technology (A)**	1.5
Voltage at peak power	17.1V	**Series resistance**	0.21Ω
Current at peak power	3.5A	**Grid voltage (V:rms)**	120V
Short-circuit current (I_{sc})	3.8A	**Grid frequency (f)**	50Hz
Open-circuit voltage (V_{oc})	21.1V	**Grid inductance line (L)**	2mH
Temperature coefficient of I_{sc} (k_1)	3mA/℃	**Grid resistor line (R)**	0.1Ω
Nominal operation cell temperature (T_{ref})	49℃	**DC bus capacitor(C)**	2200μF

Table 2. The POFO-SMC parameters

q-axis current control	$b_{11}=-1000$	ς_1=8	φ_1= 5	α_{11}= 40	α_{12}= 400
	k_{11} = 15	k_{12} = 600	$\alpha 1$ = 0.6	λ_{c1}=20	

DC link voltage control	b_{22}=−2250	ς_2=12	φ_2=10	α_{21}=30	α_{22}=300
	α_{23}=1000	k_{21}=20	k_{22}=600	k_{23}=6000	$\alpha 2 = 0.6$
	λ_{c2}=15	ϵ_o = 0.2	ϵ_c = 0.2		

5.1 Solar irradiation change

To investigate the solar irradiation change resulted from weather conditions variation, two consecutive step changes in solar irradiation are applied, which decrease from 1 kW/m^2 to 0.5 kW/m^2 at t=0.2 s and increase to 1 kW/m^2 at t=1.2 s, respectively. The temperature keeps at its rated value, e.g., 25℃, for the whole period of time. This could happen when a bird or other flying objects rapidly move above the PV cells. Meanwhile, q-axis current I_q is increased to 50 A at t=0.2 s and decreased to -30 A at t=1.2 s and finally restored to 0 A at t=1.7 s to test the power factor regulation performance. The PV system responses are illustrated in Fig. 6. It can be seen that PI control presents some DC voltage oscillations while the other nonlinear methods have no such oscillations. Moreover, POFO-SMC can track the q-axis current and track the DC link voltage at the fastest rate thanks to the beneficial combination of real-time perturbation compensation and FOSMC mechanism. Moreover, it illustrates that FOSMC owns a faster power extraction rate than that of SMC thanks to the use of fractional-order mechanism. Besides, FLC, SMC and RSMC have similar control performance since there exists no modelling/parameter uncertainties or unknown external disturbances under the studied case, so the robustness mechanism is not quite prominent. Particularly, the DC link voltage obtained by PI control reaches nearly 400V in its first overshoot when the solar irradiation decreases, which is around 12.95% lower than that of the steady-state voltage. Meanwhile, its DC link voltage reaches 600 V in its first overshoot when the solar irradiation increases, which is around 9.36% higher than that of the steady-state voltage.

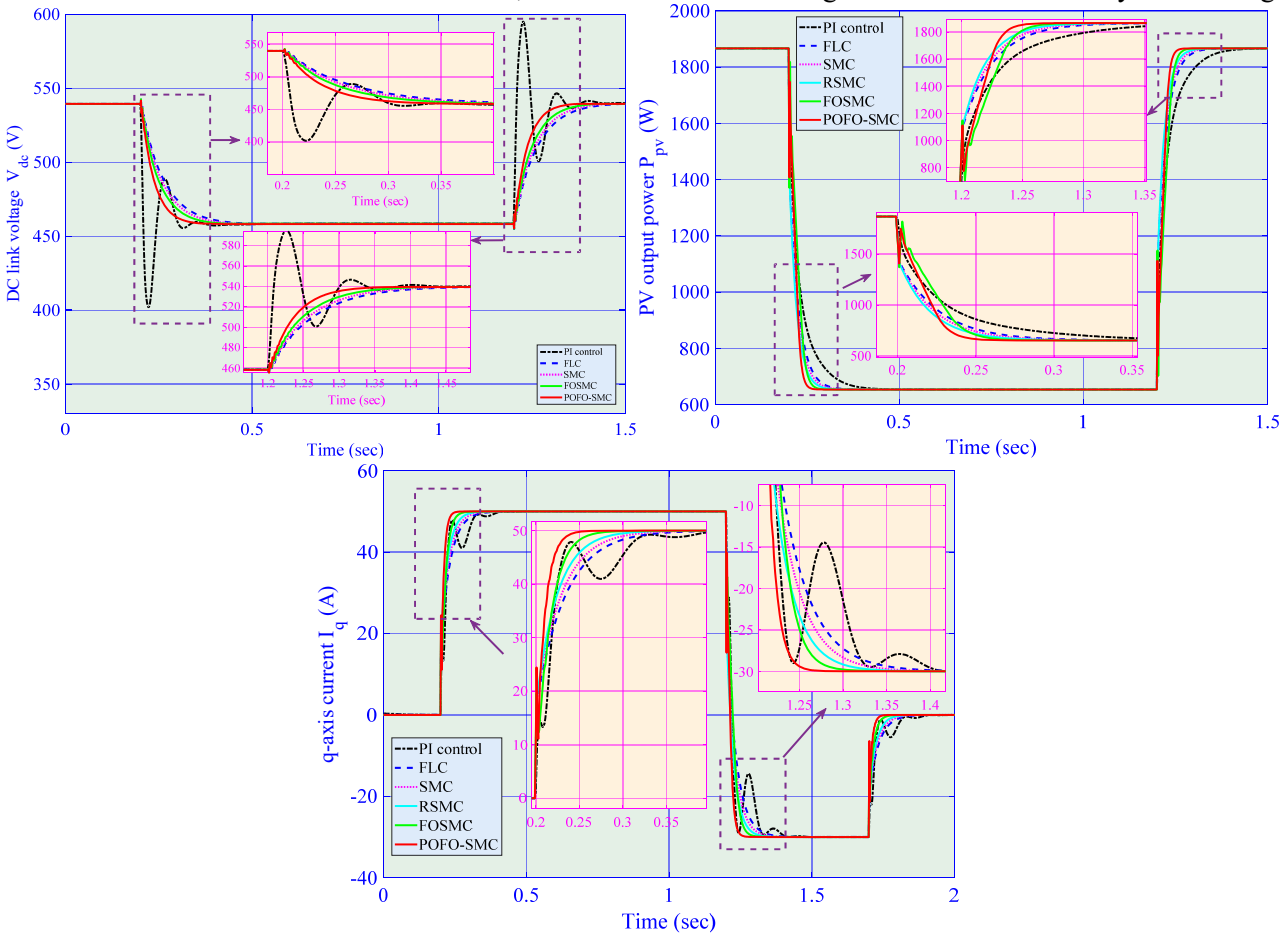

Figure 6. PV system responses obtained under step changes in solar irradiation and q-axis current regulation.

5.2 Temperature variation

Figure 7 demonstrates the PV system responses obtained under two step changes of ambient temperature at t=0.2 s from 25℃ to 40℃, and t=1.2 s from 40℃ to 25℃, while the solar irradiation is remained at 1 kW/m^2. Meanwhile, q-axis current I_q is decreased to -40 A at t=0.2 s and increased to 20 A at t=1.2 s and finally restored to 0 A at t=1.7 s. Such temperature change could be resulted in a summer day when the temperature is relatively high and some fast moving clouds cover a part of the PV panel, by which a shadow is emerged to decrease the temperature and restored when the shadow is gone. One can readily observe that POFO-SMC can achieve the most satisfactory control performance among all controllers. Again, PI control presents some oscillations in DC voltage tracking and it cannot maintain a consistent control performance when operation point varies, this is due to its essential flaws of the one-point linearization of the original nonlinear system, upon which the PI parameters are determined at a specific

operation point. When the operation condition change, the pre-desired PI parameters are likely improper or inadequate to achieve a satisfactory or desirable control performance. In some extreme cases, it may even lead to a system stability collapse. In contrast, all the nonlinear alternatives can maintain the desirable control performance as the system nonlinearities are fully removed. Lastly, they present the similar features analyzed in the previous case. Particularly, the DC link voltage obtained by PI control reaches nearly 480V in its first overshoot when the temperature increases, which is around 4.38% lower than that of the steady-state voltage. Meanwhile, its DC link voltage reaches 560V in its first overshoot when the temperature decreases, which is around 3.756% higher than that of the steady-state voltage.

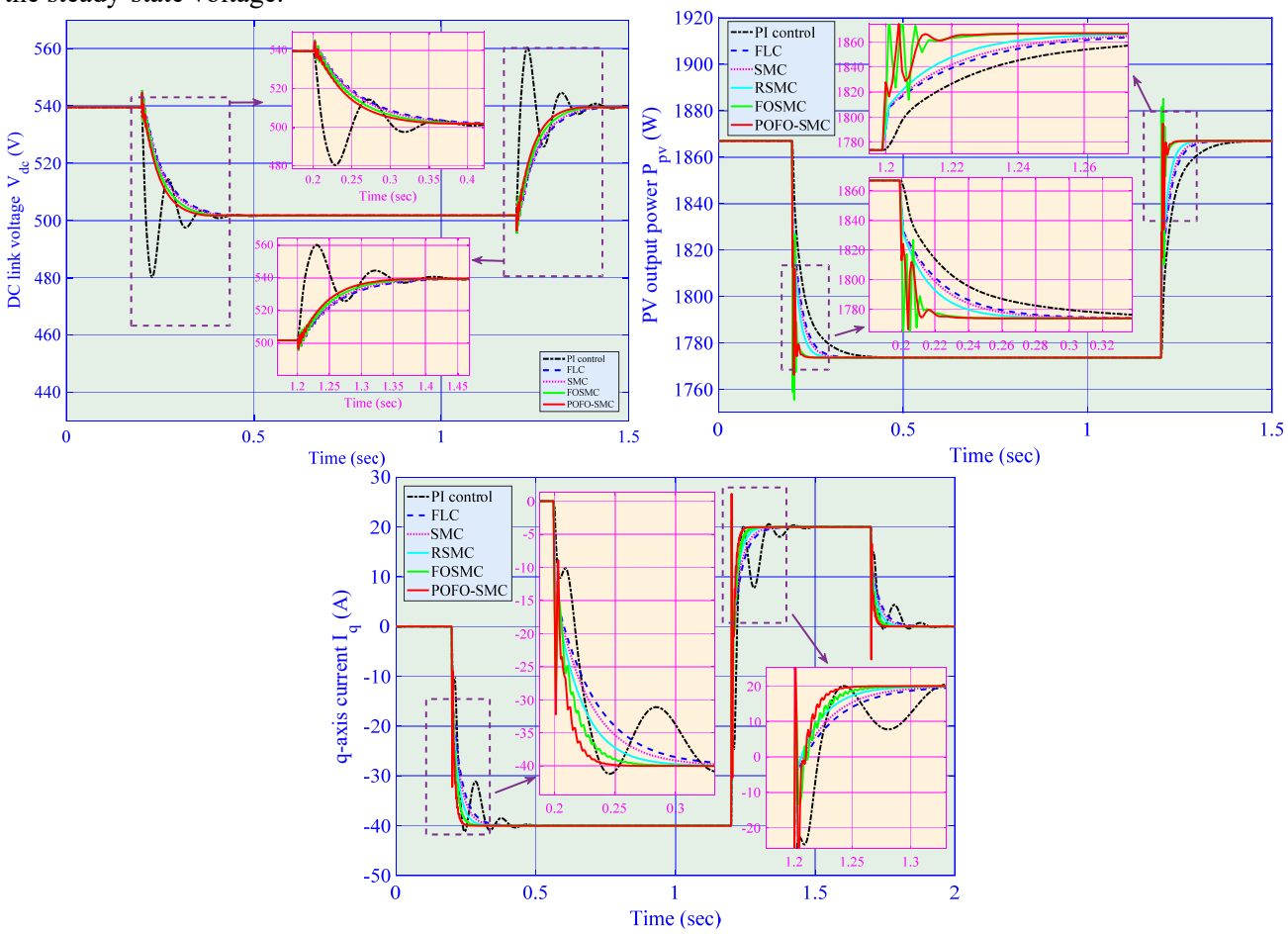

Figure 7. PV system responses obtained under temperature variation and q-axis current regulation.

5.3 Power grid voltage drop

Low-voltage ride through (LVRT) requires the PV system to stay connected and keep to generate power to the power grid under severe power grid voltage disturbances, in which the disconnection of PV system may further degrade the voltage restoration during and after fault or even cause a cascade blackout of many devices and finally result in a power system instability (Mirhosseini, Pou, & Agelidis, 2015; Wang, & Ren, 2018). As a result, a voltage drop from the rated value to 0.4 p.u. for 150 ms (t=0.2s-0.35s) (Mojallal, Lotfifard, 2017) at the standard operation condition is studied to evaluate the restoration ability of the proposed controller in comparison to that of others. The system responses are depicted in Fig. 8. It is obvious that POFO-SMC can efficiently suppress the power oscillation, DC link voltage oscillation, and q-axis current oscillation with the fastest rate and lowest overshoot as such grid disturbance could be rapidly observed and fully compensated by POFO-SMC. It also shows that PI control needs the longest time with highest overshoot to restore the disturbance, which may activate the protection device to disconnect the PV system thus it has the lowest LVRT capability. Moreover, the high-frequency power oscillation of FOSMC and POFO-SMC is due to the use of fractional-order sliding-mode mechanism, e.g., two additional control parameters. However, the magnitude of such oscillation decays very rapidly and can reach the steady state faster than that of others. In particular, when the fault occurs at 0.2 s, the magnitude of DC link voltage is about 3.34%, 1.67%, 1.30%, 0.93%, 1.02%, and 0.81% higher than the rated voltage of PI control, FLC, SMC, RSMC, FOSMC, and POFO-SMC. Meanwhile, the magnitude of output power is about 20.64%, 18.49%, 17.55%, 16.13%, 16.98%, and 19.57% higher than the rated voltage of PI control, FLC, SMC, RSMC, FOSMC, and POFO-SMC. These results shows that POFO-SMC can effectively suppress the DC voltage oscillation compared to that of other, which is due to the fact of real-

time perturbation compensation that such fault (treated as an external disturbance) is rapidly estimated and fully compensated. It is worth noting that the output power of POFO-SMC is slightly higher than that of other nonlinear approaches, together with several oscillations before restored at steady state, which is due to the emerged discontinuity of PV system parameters, e.g., line resistance, line inductance, grid voltage, such severe variation of system parameters might lead to a transient change of system states. However, SMSPO needs some time to track such change thus a relatively high magnitude of output power as well as frequent oscillations are appeared.

Furthermore, the perturbation estimation performance of SMPO and SMSPO is recorded which is illustrated in Fig. 9. As shown in Fig. 9, both SMPO and SMSPO can rapidly estimate the perturbations under the voltage drop at power grid. Note that the estimation rate of SMPO and SMSPO is mainly determined by observer gains, e.g., a larger observer gain will cause a faster tracking rate but also a higher tracking error, particularly at the beginning of a transient process like the fault studied in this case, vice versa. Besides, the thickness layer boundary of observer mainly influences the oscillation pattern of the observer, e.g., a too small value will cause a highly frequent oscillations as the sign of saturation function will reverse frequently. Furthermore, in the practical design of POFO-SMC, such high-frequency oscillation must be avoided as it might increase the heat generated by the controller thus result in additional computation costs. What's worse, in some special cases, it may even excite some resonance of the PV system which are not considered in normal operation design, such that a potential damage to the devices would be occurred.

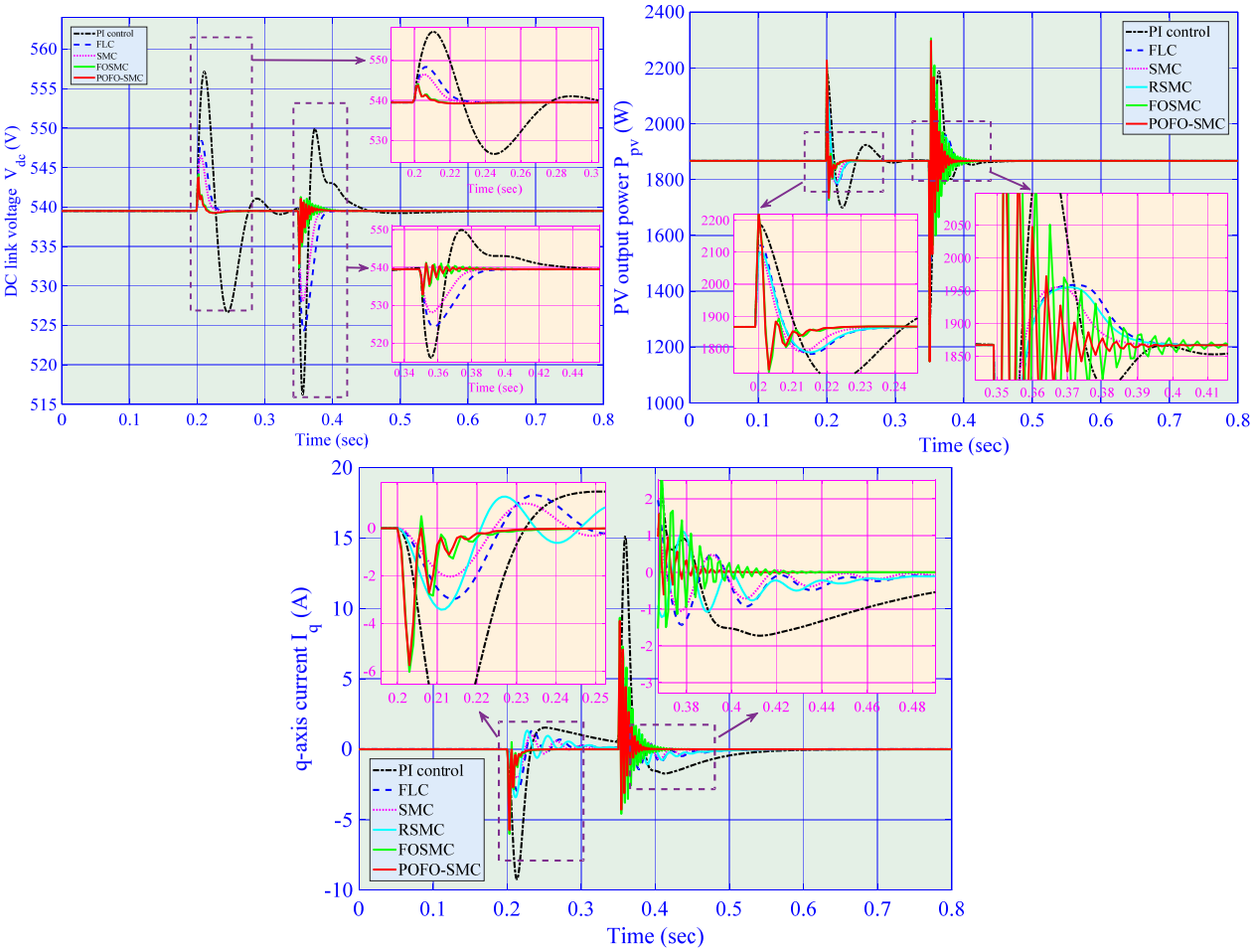

Figure 8. PV system responses obtained under the 60% voltage drop lasting 150 ms at power grid.

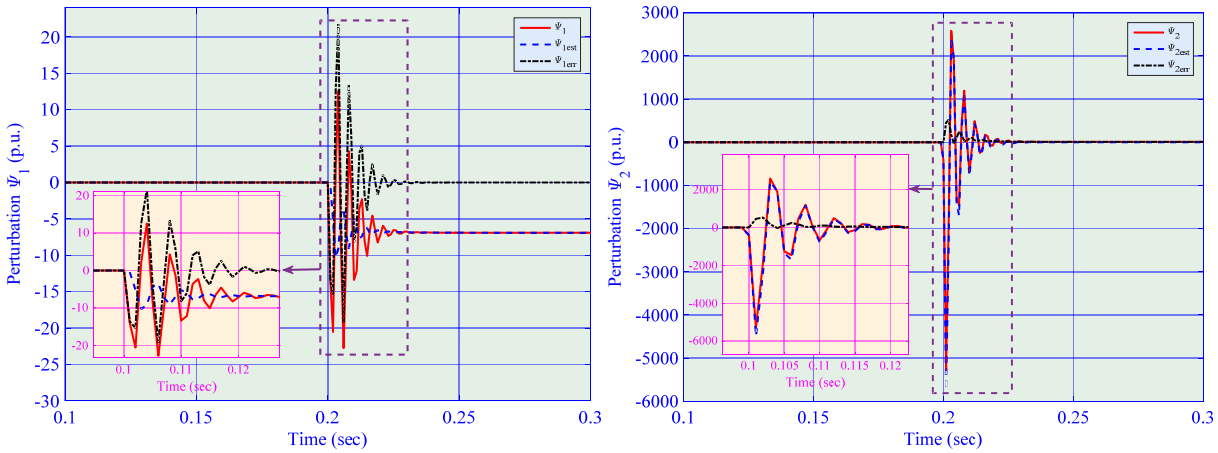

Figure 9. Perturbation estimation performance of SMPO and SMSPO obtained under the 60% voltage drop lasting 150 ms at power grid.

5.4 Inverter parameter uncertainties

In order to evaluate the robustness of POFO-SMC against to that of other control schemes in the presence of PV inverter parameter uncertainties, a series of plant-model mismatches of equivalent grid resistance R and grid inductance L within ±20% variation around their nominal value are undertaken. Note that such PV system parameter uncertainties would be occurred due to the original measurement errors, wear-and-tear, ambient temepature or air pressure change, weather condition variation, etc. As a consequence, it is worth stuying the robustness of the proposed method against such uncertainites. Here, a 0.8 p.u. three-phase voltage drop lasting 100 ms at the power grid is simulated, in which the peak value of output power $|P|$ is recorded for comparison. Figure 10 shows that the variation of peak value of active power $|P|$ obtained by PI control, FLC, SMC, RSMC, FOSMC, and POFO-SMC is 41.2%, 73.4%, 26.5%, 21.5%, 24.7%, and 18.1%, respectively. Consequently, POFO-SMC can provide the greatest robustness against to inverter parameter uncertainties thanks to the real-time compensation of perturbation, while FLC is vulnerable to parameter uncertainties as it requires an accurate PV system model. It can also be found that FLC has the lowest robustness in the presence of system parameter uncertainties, such performance is quite common and understandable for FLC as its control design requires an accurate system model in both structure and parameters. Moreover, RSMC can achieve an improved robustness than FOSMC and SMC thanks to its enhanced adaption mechanism to modelling uncertainties.

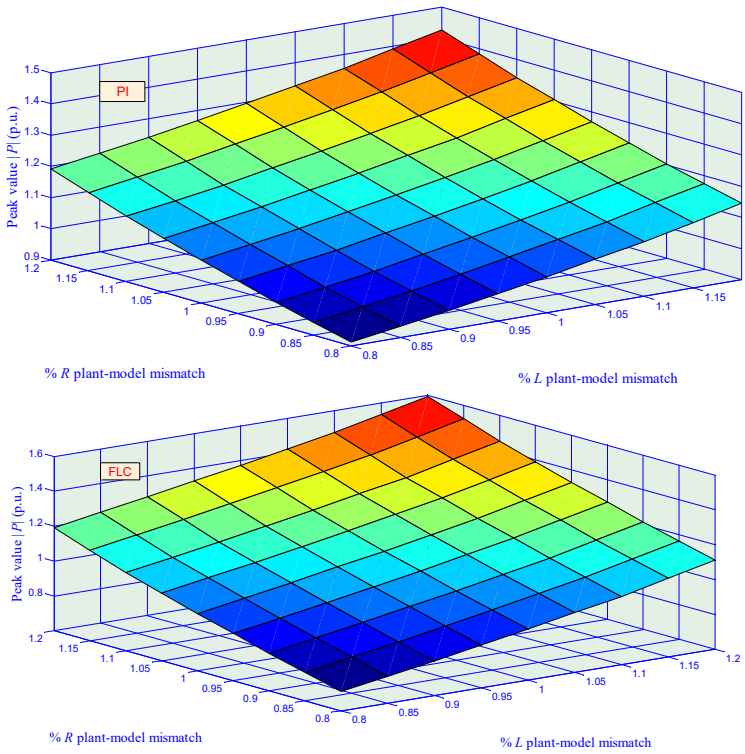

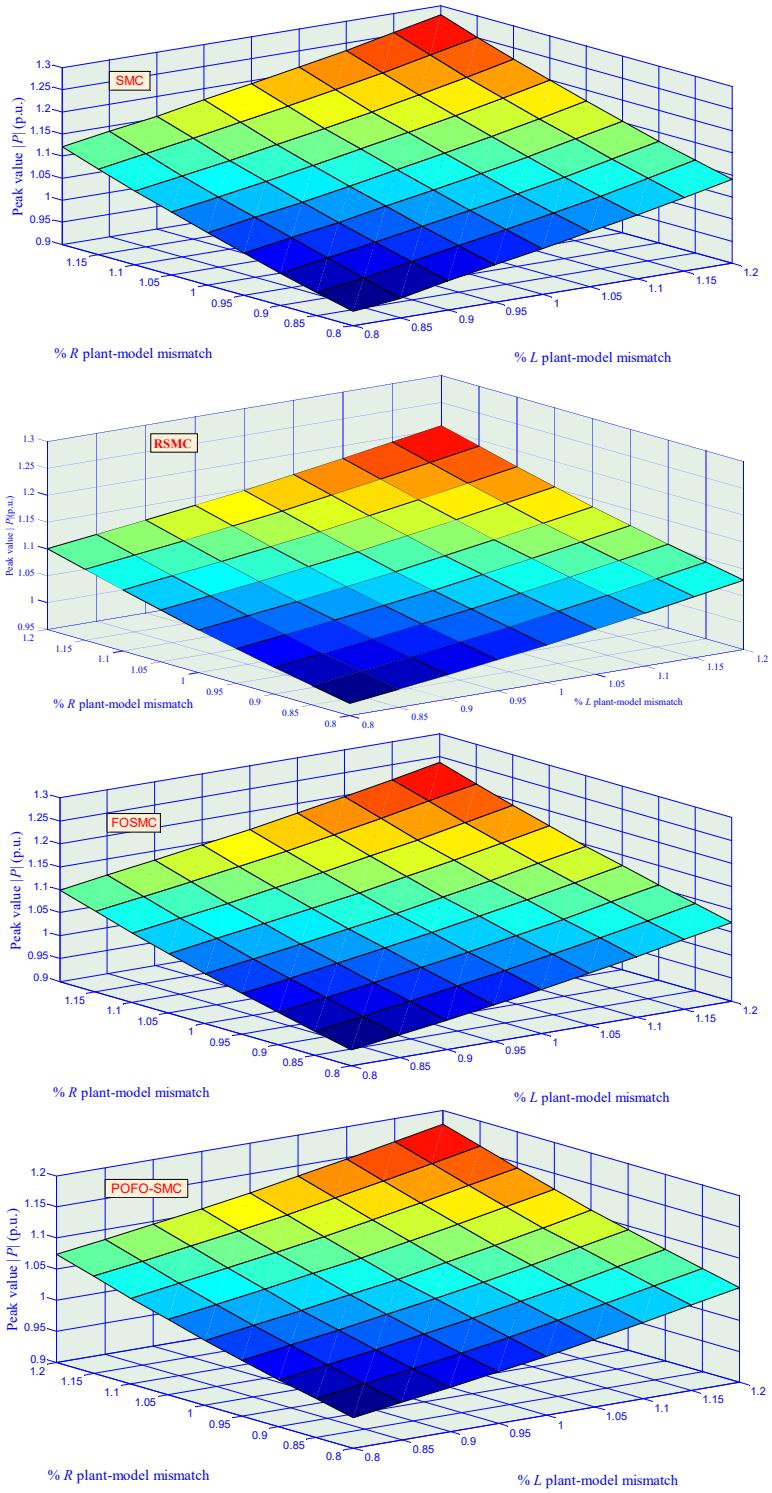

Figure 10. Peak value of active power $|P|$ obtained under a 0.8 p.u. three-phase voltage drop lasting 100 ms at power grid with 20% variation of the equivalent resistance R and inductance L of different controllers.

5.5 Statistical studies

The integral of absolute error (IAE) indices (Shen, Yao, Wen, & He, 2018; Yao, Jiang, Wen, Wu, & Cheng, 2015) of different controllers obtained in three scenarios are compared in Table 3. Here $\mathrm{IAE}_x = \int_0^T |\boldsymbol{x} - \boldsymbol{x}^*| \, \mathbf{dt}$. IAE index provides a quantitative evaluation of tracking error in a given period of time, e.g., a lower IAE index means a lower accumulated tracking error while a higher IAE index means a higher accumulated tracking error. The simulation time T=2.5 s is chosen to cover the whole operation range of all the above three scenarios. As shown in Table 3, one can readily observe that POFO-SMC owns the lowest IAE indices, thus it can outperform other control schemes thanks to the beneficial combination of perturbation compensation (enhanced robustness) and FOSMC (improved error tracking). In particular, its $\mathrm{IAE}_{\mathrm{Iq}}$ is only 58.62%, 61.14%, 63.01%, 64.73%, and 76.47% of that of PI control, FLC, SMC, RSMC, and FOSMC in the solar irradiation change. Meanwhile, its $\mathrm{IAE}_{\mathrm{Vdc}}$ is just 73.49%,

77.87%, 81.45%, 83.64%, and 87.05% of that of PI control, FLC, SMC, RMC, and FOSMC in the power grid voltage drop.

Table 3 IAE indices (in p.u.) of different controllers obtained in three scenarios.

Scenarios	IAE Indices	PI	FLC	SMC	RSMC	FOSMC	POFO-SMC
Solar irradiation change	IAE_{Iq}	0.1863	0.1786	0.1733	0.1687	0.1428	0.1092
	IAE_{Vdc}	0.4539	0.4328	0.4198	0.4056	0.3835	0.3323
Temperature variation	IAE_{Iq}	0.2283	0.2137	0.2061	0.1943	0.1742	0.1321
	IAE_{Vdc}	0.5642	0.5419	0.5287	0.5179	0.4936	0.4494
Power grid voltage drop	IAE_{Iq}	0.3467	0.3224	0.3047	0.2988	0.2843	0.2372
	IAE_{Vdc}	0.7548	0.7123	0.6810	0.6632	0.6372	0.5547

Finally, it is of great importance to investigate the overall control costs, i.e., $\int_0^T (|\boldsymbol{u_1}| + |\boldsymbol{u_2}|)\mathbf{dt}$, of each controllers required in three cases. As a practical control design should consider both the tracking performance and computational burden. From Fig. 11, one can find that POFO-SMC just requires the lowest control costs in all cases among all controllers. This is because of the mechanism of online perturbation compensation which can largely reduce the inherent over-conservativeness of SMC, such that more reasonable control costs are needed. However, based on the "No Free Lunch" Theorem, such satisfactory control perforamnce sacrifies the overall control system complexity, that is, POFO-SMC has the most complicated structure among all schemes as it contains both observer loop and controller loop, while each loop involves several derivatives and integrals, as well as fractional-order operators.

Figure 11. Overall control costs required by different controllers under three cases.

6. HIL Experiment

HIL experiment is a crucial and reliable technique to validate the complex real-time embedded systems before final hardware implementation (Mayyas, Kumar, Pisu, Rios, & Jethani, 2017), which has been widely employed in PV systems (Rezkallah, Hamadi, Chandra, & Singh, 2015; Bounechba, Bouzid, Snani, & Lashab, 2016; Kim, Kim, Ko, Jang, & Ryu, 2017) to study the implementation feasibility of various PV controllers. HIL experiment is often employed as a reliable pre-test before the final hardware implementation is undertaken.

A dSPACE based HIL experiment is carried out which configuration and experiment platform are demonstrated by Fig. 12 and Fig. 13, respectively. Here, POFO-SMC based q-axis current and DC link voltage controller (45)-(48) is embedded on one dSPACE platform (DS1104 board) with a sampling frequency f_c=1 kHz. Meanwhile, the PV system is simulated on another dSPACE platform (DS1006 board) with a limit sampling frequency f_s= 50 kHz (Yang et al., 2016; Yang et al., 2018c, 2018d). The measurements of the q-axis current i_q and DC link voltage V_{dc} are obtained from the real-time simulation of the PV system on the DS1006 board, which are sent to POFO-SMC implemented on the DS1104 board for the real-time control inputs calculation. In addition, the solar irradiation and temperature simulator is also embedded in DS1006 board, such that various atmospheric conditions could be readily applied.

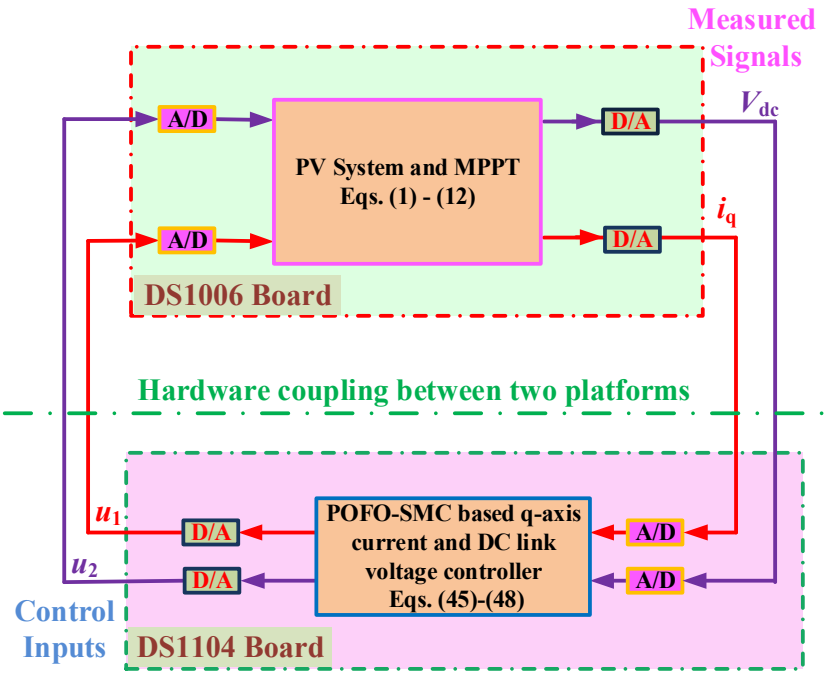

Figure 12. The schematic configuration of HIL experiment.

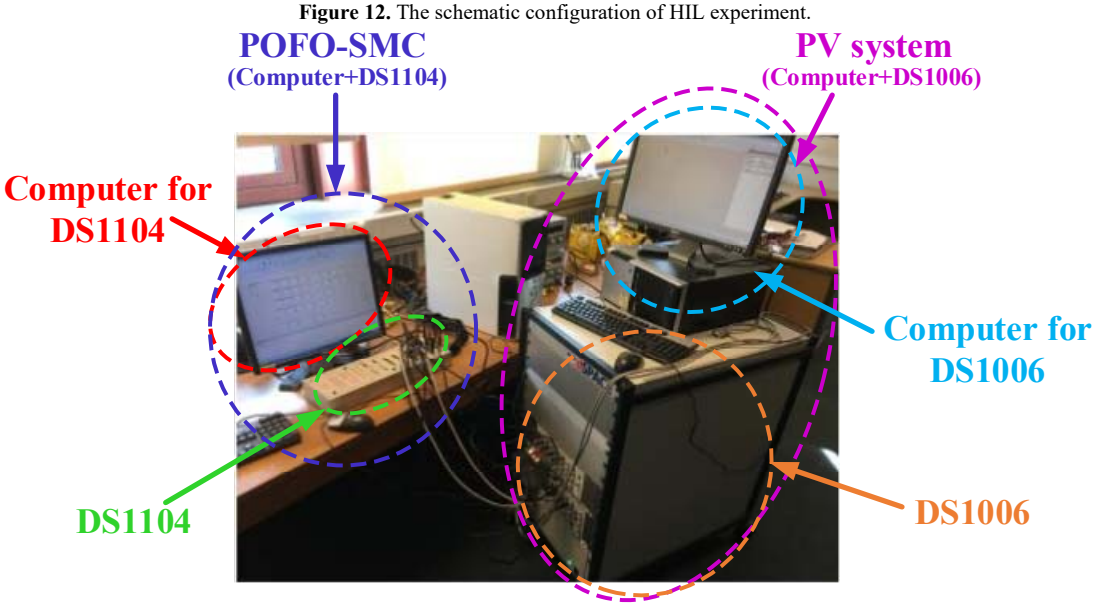

Figure 13. The hardware platform of HIL experiment.

6.1 HIL Experiment: Solar irradiation change

The system responses obtained under the simulation and HIL test are compared by Fig. 14 under the same solar irradiation change presented in Case Studies. One can observe that the results of HIL experiment and simulation are very similar. Note that there exists some consistent steady-state oscillations in HIL.

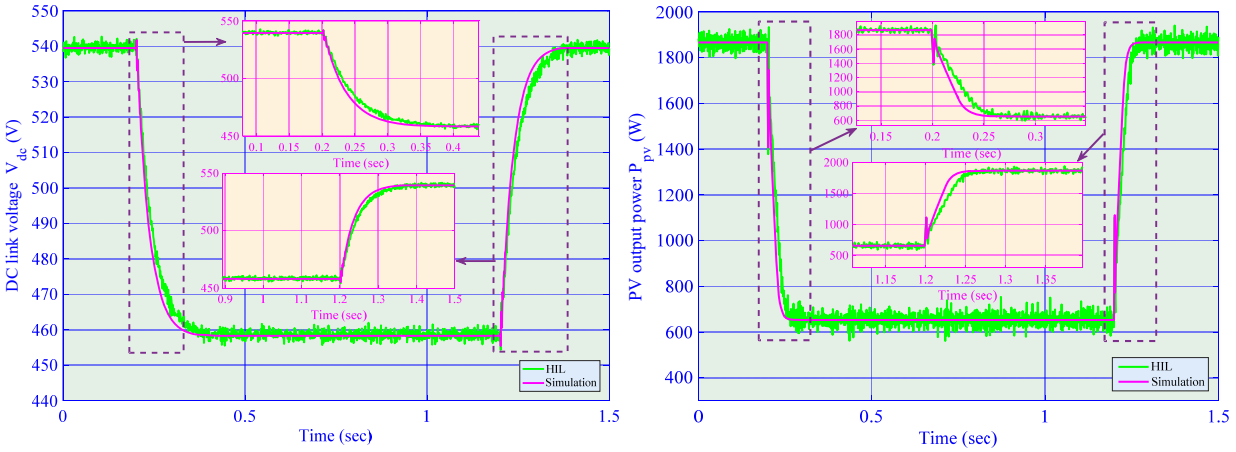

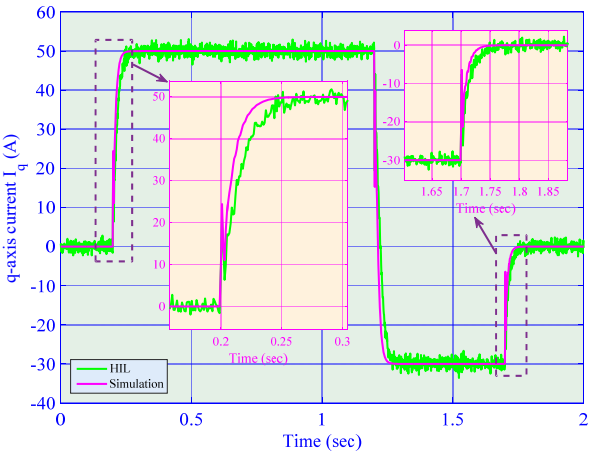

Figure 14. Simulation and HIL experiment results obtained under step changes in solar irradiation and q-axis current regulation.

6.2 HIL Experiment: Temperature variation

In the presence of the same temperature variation, Figure 15 shows that the MPPT could be rapidly achieved while HIL experiment offers almost the same results to that of simulation. The HIL experiment results are slightly slower than that of simulation.

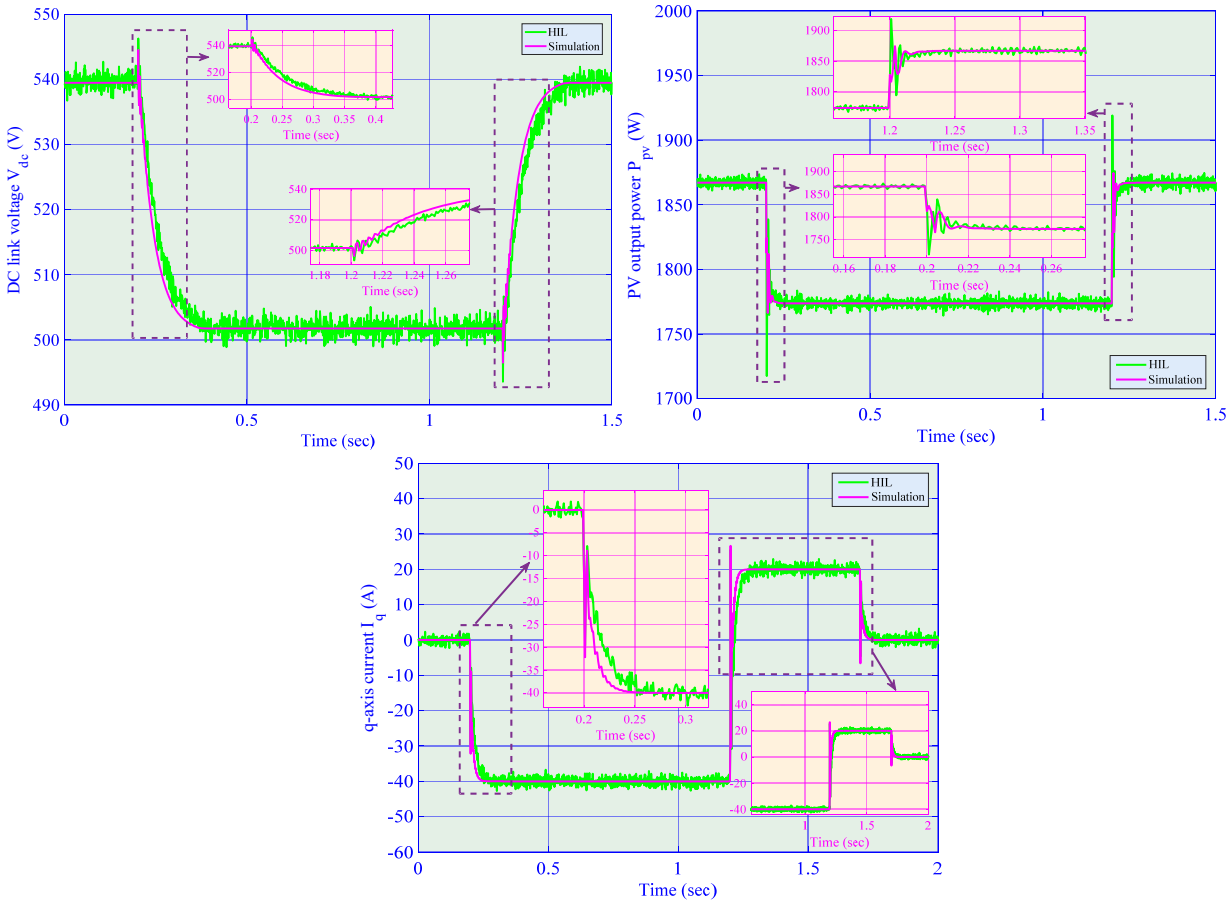

Figure 15. Simulation and HIL experiment results obtained under temperature variation and q-axis current regulation.

6.3 HIL Experiment: Power grid voltage drop

The same pattern of power grid voltage drop is studied in this study. It can be clearly seen from Fig. 16 that the HIL experiment results and simulation results match each other very well.

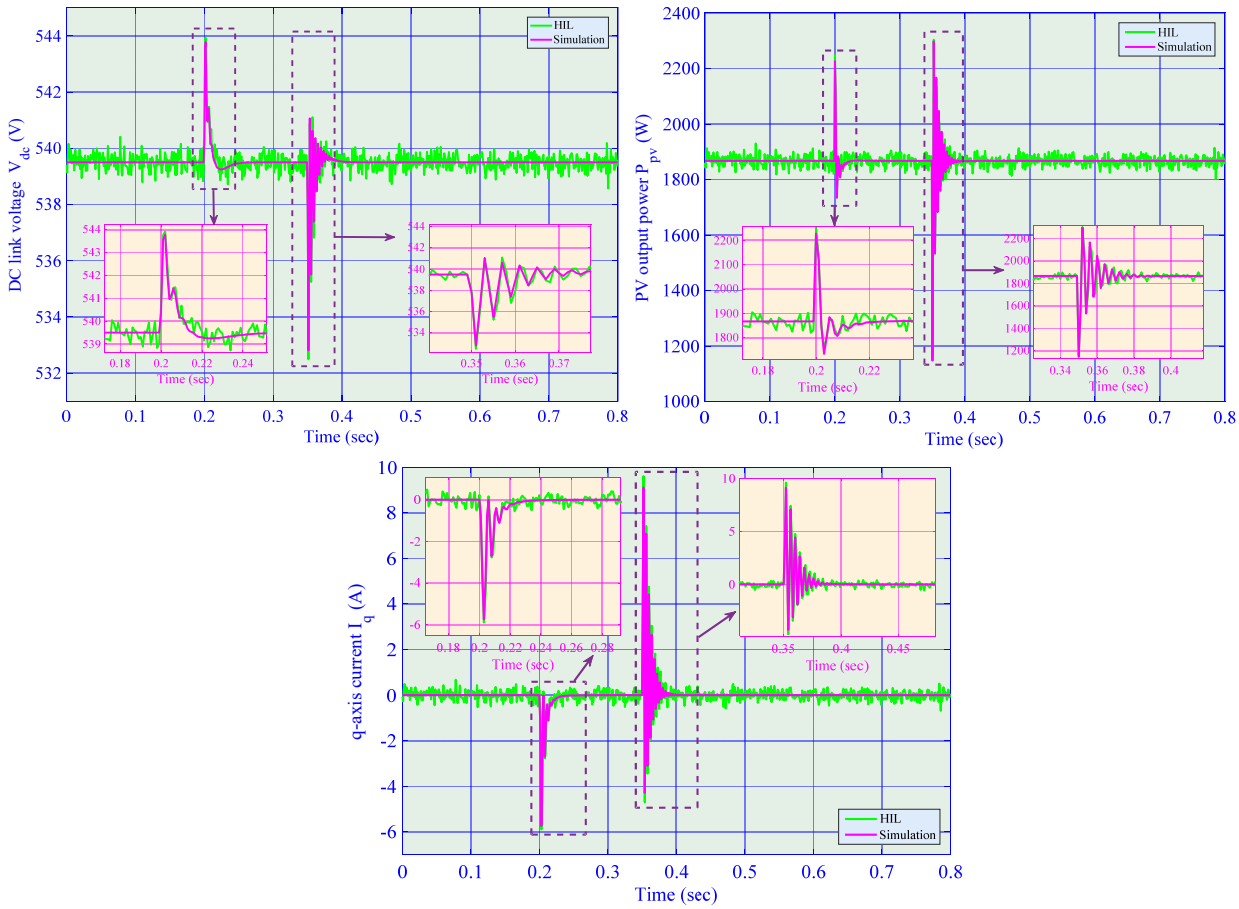

Figure 16. Simulation and HIL experiment results obtained under the 60% voltage drop lasting 150 ms at power grid.

The difference between the simulation results and HIL experiment results is mainly due to the following four reasons:

• There exist uncertain measurement disturbances in the HIL experiment which cannot be accurately considered in the simulation, which causes the consistent oscillations of the HIL experiment results. A filter could be employed to significantly remove such disturbances to improve the control performance;

• The discretization of the HIL experiment and sampling holding may introduce an additional amount of error compared to the continuous control used in the simulation;

• The existence of time delay of the real-time controller, which exact value is quite hard to obtain in practice. A time delay τ = 2 ms is assumed in the simulation. Such control signal transmission delay might cause a degradation of control performance, i.e., the HIL experiment results respond slightly slower than that of simulation results;

• Some unknown harmonics may occur in the HIL experiment caused by the capacitors or inductors between the signal transmission cables and the dSpace device.

On the other hand, for a real system, the experiment results will be even more deviated from the simulation results. The limitations due to various real-life factors are given as follows:

• Control bandwidth: A small bandwidth will restrict the transmission completeness of control signal, i.e., the information of control signals which are not located in the bandwidth will be lost to some extent, while a larger deviation from the bandwidth will cause more signal losses. This usually leads to a further degradation of control performance in both tracking rate and accuracy;

• ADC delays and other delays: These delays may significantly degrade the control performance in both tracking rate and accuracy;

• Chattering: It will bring in more noises into the experiment results, particularly in the steady state.

7. Discussions

7.1 MPPT performance comparison

The adopted MPPT is VSINC algorithm (Li & Wang, 2009). Recently, artificial intelligence (AI) methods provide an efficient MPPT of PV system. In this section, adaptive neuro-fuzzy inference system (ANFIS) (Kharb, Shimi, Chatterji, & Ansari, 2014) is used for MPPT and compared to that of VSINC algorithm.

The start-up test is carried out with initial voltage V_{dc}=60 V, current I_{pv}=0 A, and power P=0 W. The two algorithms are applied to seek the MPP, and finally reach the rated solar irradiation and temperature (Their values

have been given in Section 5), respectively. Figure 17 illustrates the MPPT performance obtained by both VSINC and ANFIS. From Fig. 17, one can find that ANFIS owns a faster tracking rate of MPP against VSINC. Moreover, ANFIS can significantly reduce the steady-state oscillation compared to that of VSINC, which is an inherent flaw of conventional MPPT techniques (Kandemir, Cetin, & Borekci, 2017). In contrast, VSINC has a quite simple structure for easy implementation, which has been widely used in practice. To summarize, VSINC can achieve an improved MPPT performance but also need a more complicated structure in comparison to that of VSINC.

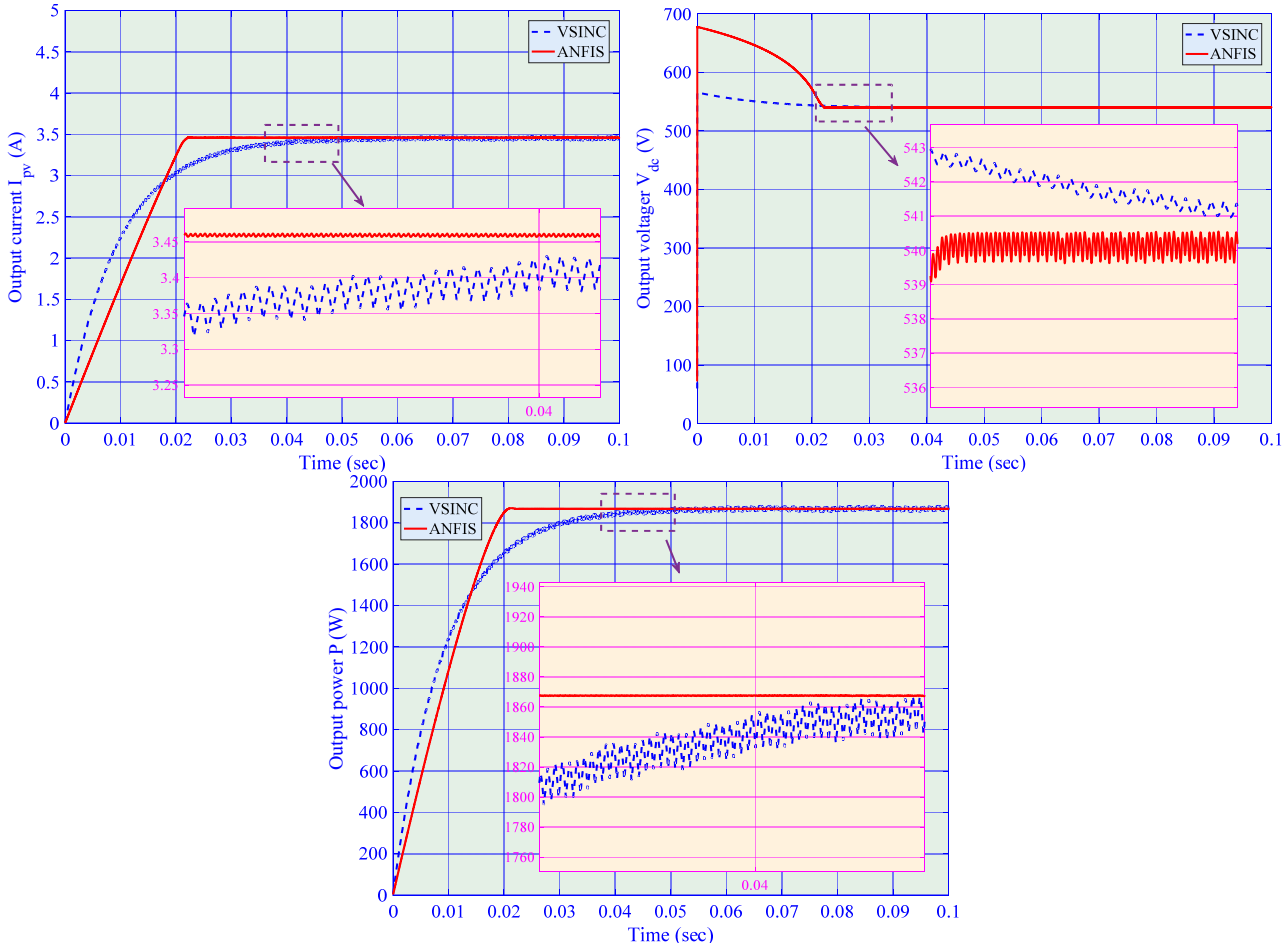

Figure 17. MPPT performance obtained under start-up test by VSINC and ANFIS.

7.2 Integration of Hierarchical droop-based control framework

It is worth noting that POFO-SMC design in this paper is at the device-level control. In the case of system-level control, it needs to be integrated into the hierarchical droop-based control framework to join the overall frequency regulation or reactive regulation of the power systems/microgrids. The hierarchical droop-based control framework can be generally classified into the following four levels (Baghaee, Mirsalim, Gharehpetian, et al., 2016a, 2016b, 2016c, 2018a, 2018b; Guerrero, et al., 2010, 2013):

(1) Level 3 (Tertiary control): This level is regarded as the energy-production level, which attempts to control the power flow between the microgrids and the power grid;

(2) Level 2 (Secondary control): This level ensures that the electrical levels into the microgrids are within the required values. Generally speaking, it could involves a synchronization control loop to smoothly connect or disconnect the microgrids to or from the distribution systems;

(3) Level 1 (Primary control): This level often adopts various droop-control methods to simulate the physical behaviours that cam lead the system stable and well damped. In addition, it could include a virtual impedance control loop for the emulation of the physical output impedance;

(4) Level 0 (Inner control loops): This level focuses on the module/device realization, including current and voltage, feedback and feedforward, etc. Meanwhile, either linear control or nonlinear control loops can be adopted for the regulation of the output voltage, as well as maintaining the system stability and current regulation.

Based on the above framework, POFO-SMC is applied on Level 0 (inner control loops), which control command is obtained from the higher level of the system, such that the controlled devices can achieve the overall control goal made by power companies/enterprises/plants. This can be directly done as POFO-SMC does not require an accurate PV system model and only needs the q-axis current reference and DC voltage reference sent by higher levels, such that an improved control performance can be realized under the hierarchical droop-based control of the whole system.

7.3 POFO-SMC Redesign for current-control mode

If the PV inverter is current-source converter (CSC) (Sahan, Vergara, Henze, Engler, & Zacharias, 2008) instead of the VSC, POFO-SMC needs to be redesigned for such PV systems. The CSC based PV inverter dynamics is described as follows:

$$\begin{cases} I_{\mathrm{d}} = \frac{e_{\mathrm{d}}}{R} + i_{\mathrm{d}} + C\frac{\mathrm{d}e_{\mathrm{d}}}{\mathrm{d}t} + \omega C e_{\mathrm{q}} \\ I_{\mathrm{q}} = \frac{e_{\mathrm{q}}}{R} + i_{\mathrm{q}} + C\frac{\mathrm{d}e_{\mathrm{q}}}{\mathrm{d}t} - \omega C e_{\mathrm{d}} \end{cases} \tag{50}$$

$$L_{\mathrm{dc}}\frac{\mathrm{d}I_{\mathrm{pv}}}{\mathrm{d}t} = \frac{e_{\mathrm{d}}i_{\mathrm{d}} + e_{\mathrm{q}}i_{\mathrm{q}}}{I_{\mathrm{pv}}} - R_{\mathrm{dc}}I_{\mathrm{pv}} \tag{51}$$

Define the state vector as $x = (x_1, x_2, x_3)^{\mathrm{T}} = \left(e_{\mathrm{d}}, e_{\mathrm{q}}, I_{\mathrm{pv}}\right)^{\mathrm{T}}$, system output $y = (y_1, y_2)^{\mathrm{T}} = \left(e_{\mathrm{q}}, I_{\mathrm{pv}}\right)^{\mathrm{T}}$, and control input $u = (u_1, u_2)^{\mathrm{T}} = \left(I_{\mathrm{d}}, I_{\mathrm{q}}\right)^{\mathrm{T}}$, respectively. The state equation of CSC based PV inverter (50) and (51) can be written as

$$\dot{x} = f(x) + g(x)u \tag{52}$$

where

$$f(x) = \begin{pmatrix} f_1 \\ f_2 \\ f_3 \end{pmatrix} = \begin{pmatrix} -\frac{x_1}{RC} - \omega x_2 - \frac{i_{\mathrm{d}}}{C} \\ -\frac{x_2}{RC} + \omega x_1 - \frac{i_{\mathrm{q}}}{C} \\ \frac{i_{\mathrm{d}}x_1 + i_{\mathrm{q}}x_2}{L_{\mathrm{dc}}x_3} - \frac{R_{\mathrm{dc}}}{L_{\mathrm{dc}}}x_3 \end{pmatrix}; \qquad g(x) = \begin{pmatrix} \frac{1}{C} & 0 \\ 0 & \frac{1}{C} \\ 0 & 0 \end{pmatrix} \tag{53}$$

Differentiate the output y until control input u appears explicitly, yields

$$\begin{cases} \dot{y}_1 = -\frac{e_{\mathrm{q}}}{RC} + \omega e_{\mathrm{d}} - \frac{i_{\mathrm{q}}}{C} + \frac{u_2}{C} \\ \ddot{y}_2 = \frac{R_{\mathrm{dc}}^2}{L_{\mathrm{dc}}^2}I_{\mathrm{pv}} - \frac{(e_{\mathrm{d}}i_{\mathrm{d}} + e_{\mathrm{q}}i_{\mathrm{q}})^2}{L_{\mathrm{dc}}^2 I_{\mathrm{pv}}^3} - \frac{i_{\mathrm{d}}^2 + i_{\mathrm{q}}^2}{L_{\mathrm{dc}}CI_{\mathrm{pv}}} - \frac{(e_{\mathrm{d}}i_{\mathrm{d}} + e_{\mathrm{q}}i_{\mathrm{q}})}{L_{\mathrm{dc}}RCI_{\mathrm{pv}}} + \frac{\omega(e_{\mathrm{q}}i_{\mathrm{q}} - e_{\mathrm{d}}i_{\mathrm{d}})}{L_{\mathrm{dc}}I_{\mathrm{pv}}} + \frac{i_{\mathrm{d}}}{L_{\mathrm{dc}}CI_{\mathrm{pv}}}u_1 + \frac{i_{\mathrm{q}}}{L_{\mathrm{dc}}CI_{\mathrm{pv}}}u_2 \end{cases} \tag{54}$$

System (54) can be rewritten into the following matrix form

$$\begin{bmatrix} \dot{y}_1 \\ \ddot{y}_2 \end{bmatrix} = \begin{bmatrix} h_1(x) \\ h_2(x) \end{bmatrix} + B(x)\begin{bmatrix} u_1 \\ u_2 \end{bmatrix} \tag{55}$$

where

$$h_1(x) = -\frac{e_{\mathrm{q}}}{RC} + \omega e_{\mathrm{d}} - \frac{i_{\mathrm{q}}}{C} \tag{56}$$

$$h_2(x) = \frac{R_{\mathrm{dc}}^2}{L_{\mathrm{dc}}^2}I_{\mathrm{pv}} - \frac{(e_{\mathrm{d}}i_{\mathrm{d}} + e_{\mathrm{q}}i_{\mathrm{q}})^2}{L_{\mathrm{dc}}^2 I_{\mathrm{pv}}^3} - \frac{i_{\mathrm{d}}^2 + i_{\mathrm{q}}^2}{L_{\mathrm{dc}}CI_{\mathrm{pv}}} - \frac{(e_{\mathrm{d}}i_{\mathrm{d}} + e_{\mathrm{q}}i_{\mathrm{q}})}{L_{\mathrm{dc}}RCI_{\mathrm{pv}}} + \frac{\omega(e_{\mathrm{q}}i_{\mathrm{q}} - e_{\mathrm{d}}i_{\mathrm{d}})}{L_{\mathrm{dc}}I_{\mathrm{pv}}} \tag{57}$$

with

$$B(x) = \begin{bmatrix} 0 & \frac{1}{C} \\ \frac{i_{\mathrm{d}}}{L_{\mathrm{dc}}CI_{\mathrm{pv}}} & \frac{i_{\mathrm{q}}}{L_{\mathrm{dc}}CI_{\mathrm{pv}}} \end{bmatrix} \tag{58}$$

The inverse of control gain matrix $B(x)$ is then calculated by

$$B^{-1}(x) = \begin{bmatrix} -\frac{Ci_{\mathrm{q}}}{i_{\mathrm{d}}} & \frac{L_{\mathrm{dc}}CI_{\mathrm{pv}}}{i_{\mathrm{d}}} \\ C & 0 \end{bmatrix} \tag{59}$$

In order to ensure the above input-output linearization to be valid, the control gain matrix $B(x)$ must be nonsingular among the whole operation range, which obtains

$$\det[B(x)] = -\frac{i_{\mathrm{d}}}{L_{\mathrm{dc}}C^2I_{\mathrm{pv}}} \neq 0 \tag{60}$$

Since the d-axis component of grid voltage i_{d} is always different from zero under the whole operation range, the above condition can be always satisfied.

Assume all the nonlinearities and parameters of PV systems are unknown, define the perturbations $\psi_1(\cdot)$ and $\psi_2(\cdot)$ for PV system (54), as follows:

$$\begin{bmatrix} \psi_1(\cdot) \\ \psi_2(\cdot) \end{bmatrix} = \begin{bmatrix} h_1(x) \\ h_2(x) \end{bmatrix} + (B(x) - B_0)\begin{bmatrix} u_1 \\ u_2 \end{bmatrix} \tag{61}$$

with the constant control gain matrix B_0 being given by

$$B_0 = \begin{bmatrix} b_{11} & 0 \\ 0 & b_{22} \end{bmatrix} \tag{62}$$

where b_{11} and b_{22} are the constant control gains. Here, matrix B_0 is chosen in the diagonal form to fully decouple the control of q-axis voltage e_{q} and PV cell current I_{pv}.

Define the tracking error $e = [e_1, e_2]^{\mathrm{T}} = [e_{\mathrm{q}}\text{-}e_{\mathrm{q}}^*, I_{\mathrm{pv}}\text{-}I_{\mathrm{pv}}^*]^{\mathrm{T}}$, where q-axis voltage reference e_{q}^* is given by the power grid operator while PV cell current reference I_{pv}^* is determined by VSINC based MPPT technique shown in Fig. 4. Differentiate the tracking error e until the control input u appears explicitly, it gives

$$\begin{bmatrix} \dot{e}_1 \\ \ddot{e}_2 \end{bmatrix} = \begin{bmatrix} \psi_1(\cdot) \\ \psi_2(\cdot) \end{bmatrix} + B_0 \begin{bmatrix} u_1 \\ u_2 \end{bmatrix} - \begin{bmatrix} \dot{e}_{\mathrm{q}}^* \\ \ddot{I}_{\mathrm{pv}}^* \end{bmatrix} \tag{63}$$

A second-order SMPO is used to estimate perturbation $\psi_1(\cdot)$ as

$$\begin{cases} \dot{\hat{e}}_{\mathrm{q}} = \hat{\psi}_1(\cdot) + \alpha_{11}\tilde{e}_{\mathrm{q}} + k_{11}\mathrm{sat}(\tilde{e}_{\mathrm{q}}, \epsilon_{\mathrm{o}}) + b_{11}u_1 \\ \dot{\hat{\psi}}_1(\cdot) = \alpha_{12}\tilde{e}_{\mathrm{q}} + k_{12}\mathrm{sat}(\tilde{e}_{\mathrm{q}}, \epsilon_{\mathrm{o}}) \end{cases} \tag{64}$$

where observer gains k_{11}, k_{12}, α_{11}, and α_{12}, are all positive constants.

Meanwhile, a third-order SMSPO is adopted to estimate perturbation $\psi_2(\cdot)$ as

$$\begin{cases} \dot{\hat{I}}_{\mathrm{pv}} = \hat{\dot{I}}_{\mathrm{pv}} + \alpha_{21}\tilde{I}_{\mathrm{pv}} + k_{21}\mathrm{sat}(\tilde{I}_{\mathrm{pv}}, \epsilon_{\mathrm{o}}) \\ \hat{\dot{I}}_{\mathrm{pv}} = \hat{\psi}_2(\cdot) + \alpha_{22}\tilde{I}_{\mathrm{pv}} + k_{22}\mathrm{sat}(\tilde{I}_{\mathrm{pv}}, \epsilon_{\mathrm{o}}) + b_{22}u_2 \\ \dot{\hat{\psi}}_2(\cdot) = \alpha_{23}\tilde{I}_{\mathrm{pv}} + k_{23}\mathrm{sat}(\tilde{I}_{\mathrm{pv}}, \epsilon_{\mathrm{o}}) \end{cases} \tag{65}$$

where observer gains k_{21}, k_{22}, k_{23}, α_{21}, α_{22}, and α_{23}, are all positive constants.

The fractional-order PD$^{\alpha}$ sliding surface of tracking error dynamics (54) is chosen as

$$\begin{bmatrix} \hat{S}_{\mathrm{FO1}} \\ \hat{S}_{\mathrm{FO2}} \end{bmatrix} = \begin{bmatrix} \mathrm{D}^{\alpha 1}(\hat{e}_{\mathrm{q}} - e_{\mathrm{q}}^*) + \lambda_{\mathrm{c1}}(\hat{e}_{\mathrm{q}} - e_{\mathrm{q}}^*) \\ \mathrm{D}^{\alpha 2}(\hat{I}_{\mathrm{pv}} - I_{\mathrm{pv}}^*) + \lambda_{\mathrm{c2}}(\hat{I}_{\mathrm{pv}} - I_{\mathrm{pv}}^*) \end{bmatrix} \tag{66}$$

where $\alpha 1$ and $\alpha 2$ are the operation orders, positive constants λ_{c1} and λ_{c2} denote the fractional-order PD$^{\alpha}$ sliding surface gains. The attractiveness of fractional-order PD$^{\alpha}$ sliding surface (66) guarantees the q-axis voltage e_{q} and PV cell current I_{pv} can effectively track to their reference.

The POFO-SMC for CSC based PV system (54) can now be designed as

$$\begin{bmatrix} u_1 \\ u_2 \end{bmatrix} = B_0^{-1} \begin{bmatrix} \dot{e}_{\mathrm{q}}^* - \hat{\psi}_1(\cdot) - \varsigma_1 \hat{S}_{\mathrm{FO1}} - \varphi_1 \mathrm{sat}(\hat{S}_{\mathrm{FO1}}, \epsilon_{\mathrm{c}}) \\ \ddot{I}_{\mathrm{pv}}^* - \hat{\psi}_2(\cdot) - \varsigma_2 \hat{S}_{\mathrm{FO2}} - \varphi_2 \mathrm{sat}(\hat{S}_{\mathrm{FO2}}, \epsilon_{\mathrm{c}}) \end{bmatrix} \tag{67}$$

where positive sliding-mode control gains ς_1, ς_2, φ_1, and φ_2 are chosen to ensure the convergence of tracking error dynamics (54).

8. Conclusions

In this paper, a novel POFO-SMC scheme is proposed for grid-connected PV inverter to extract the available maximum power from solar energy under various atmospheric conditions, while the main conclusions can be drawn into the following five folds:

(1) An SMSPO is employed to simultaneously estimate the combinatorial effect of PV inverter nonlinearities and parameter uncertainties, unmodelled dynamics, stochastic fluctuation of atmospheric conditions, and external disturbances online, which is fully compensated by an FOSMC to realize a globally consistent control performance and to considerably enhance the system robustness;

(2) The error tracking performance is greatly enhanced thanks to the use of fractional-order PD$^{\alpha}$ sliding surface. Moreover, the inherent over-conservativeness of SMC/FOSMC is noticeably reduced as the upper bound of perturbation is replaced by its real-time estimate, such that a more reasonable control costs can be resulted in;

(3) POFO-SMC does not require an accurate PV system model while only the measurement of DC link voltage and q-axis current is required. Furthermore, the control of DC link voltage and q-axis current is fully decoupled through the selection of a diagonal constant control gain matrix. Therefore, POFO-SMC is relatively easy to be implemented in practice compared to other nonlinear controllers;

(4) Simulation results of case studies verify that POFO-SMC can achieve a globally consistent control performance while satisfactorily extract the available maximum solar energy under different weather conditions, together with the lowest overall control costs among all cases;

(5) The hardware implementation feasibility of POFO-SMC is validated through dSpace based HIL experiment.

Future studies will attempt to adopt meta-heuristic optimization algorithms for (a) global MPP seeking under non-uniform solar irradiation conditions and (b) search the optimal control parameters of POFO-SMC.

Appendix A. Proof of Robustness

Note that the robustness of POFO-SMC is determined by the estimation error convergence of SMSPO, more specifically, the real-time compensation of perturbation estimate ensures the robustness of the proposed controller as

the combinatorial effect of various uncertainties, unmodelled dynamics and external disturbances are all aggregated by the perturbation. The estimation error convergence of SMSPO is proved as follows:

Firstly, subtracting SMSPO (18) from extended system (17), one can obtain the estimation error of SMSPO as

$$\begin{cases} \dot{\tilde{x}}_1 = \tilde{x}_2 - \alpha_1\tilde{x}_1 - k_1\mathrm{sat}(\tilde{x}_1) \\ \quad\vdots \\ \dot{\tilde{x}}_n = \tilde{x}_{n+1} - \alpha_n\tilde{x}_1 - k_n\mathrm{sat}(\tilde{x}_1) \\ \dot{\tilde{x}}_{n+1} = -\alpha_{n+1}\tilde{x}_1 - k_{n+1}\mathrm{sat}(\tilde{x}_1) + \dot{\Psi}(\cdot) \end{cases} \tag{A1}$$

The sliding surface is defined as $S_{\mathrm{spo}}(\tilde{x}) = \tilde{x}_1 = 0$. Construct a Lyapunov candidate function $V_{\mathrm{spo}} = \frac{1}{2}S_{\mathrm{spo}}^2$, the sliding surface is attractive if $\dot{V}_{\mathrm{spo}} < 0$ for $\tilde{x} \notin S_{\mathrm{spo}}$. Moreover, the existence of sliding mode is determined by

$$\begin{cases} \tilde{x}_2 \le k_1 + \alpha_1\tilde{x}_1, \text{ if } \tilde{x}_1 > 0; \\ \tilde{x}_2 \ge -k_1 + \alpha_1\tilde{x}_1, \text{ if } \tilde{x}_1 < 0. \end{cases} \tag{A2}$$

The above condition can be guaranteed by choosing k_1 as equation (20).

Moreover, the reduced estimation error dynamics on the sliding mode can be written as Jiang et al. (2002)

$$\begin{cases} \dot{\tilde{x}}_2 = -\frac{k_2}{k_1}\tilde{x}_2 + \tilde{x}_3 \\ \dot{\tilde{x}}_3 = -\frac{k_3}{k_1}\tilde{x}_2 + \tilde{x}_4 \\ \quad\vdots \\ \dot{\tilde{x}}_n = -\frac{k_n}{k_1}\tilde{x}_2 + \tilde{x}_n \\ \dot{\tilde{x}}_{n+1} = -\frac{k_{n+1}}{k_1}\tilde{x}_2 + \dot{\Psi}(\cdot) \end{cases} \tag{A3}$$

or

$$\dot{\tilde{x}}_{\mathrm{e1}} = A_1\tilde{x}_{\mathrm{e1}} + B_1\dot{\Psi}(\cdot) \tag{A4}$$

where $\tilde{x}_{\mathrm{e1}} = [\tilde{x}_2 \cdots \tilde{x}_{n+1}]^T$, and $n \times n$ matrix A_1 and $n \times 1$ matrix B_3 are as follows

$$A_1 = \begin{bmatrix} -\frac{k_2}{k_1} & 1 & \cdots & \cdots & 0 \\ -\frac{k_3}{k_1} & 0 & 1 & \cdots & 0 \\ \vdots & & & & \vdots \\ -\frac{k_n}{k_1} & 0 & 0 & \cdots & 1 \\ -\frac{k_{n+1}}{k_1} & 0 & 0 & \cdots & 0 \end{bmatrix},\ B_3 = \begin{bmatrix} 0 \\ \vdots \\ 0 \\ 1 \end{bmatrix} \tag{A5}$$

Define the state transformation as

$$\tilde{x}_i = \lambda_{\mathrm{k}}^{i-2} z_i,\ i = 2, \cdots, n+1 \tag{A6}$$

Then, equation (A4) can be written in terms of z as

$$\dot{z} = \lambda_{\mathrm{k}} M z + B_1 \frac{\dot{\Psi}(\cdot)}{\lambda_{\mathrm{k}}^{n-1}} \tag{A7}$$

where $z = [z_2\ \cdots\ z_{n+1}]^{\mathrm{T}}$, and $n \times n$ matrix M is written as

$$M = \begin{bmatrix} -C_n^1 & 1 & \cdots & \cdots & 0 \\ -C_n^2 & 0 & 1 & \cdots & 0 \\ \vdots & & & & \vdots \\ -C_n^{n-1} & 0 & 0 & \cdots & 1 \\ -C_n^n & 0 & 0 & \cdots & 0 \end{bmatrix} \tag{A8}$$

Define the Lyapunov function

$$W_1 = \frac{1}{\lambda_{\mathrm{k}}}\, z^T P_1 z \tag{A9}$$

where P_1 is the positive definite solution of the Lyapunov equation $P_1 M + M^T P_1 = -I$. Differentiating W_1 along system (A7) one obtains

$$\dot{W}_1 = -\|z\|^2 + 2z^T \frac{P_1}{\lambda_{\mathrm{k}}} B_1 \frac{\dot{\Psi}(\cdot)}{\lambda_{\mathrm{k}}^{n-1}} \tag{A10}$$

using the assumption A.2, one can assume $\dot{\Psi}(\cdot) \le \gamma_2$ can be rewritten as

$$\dot{W}_1 \le -\|z\|^2 + \frac{2\lambda_{\max}(P_1)\|z\|\gamma_2}{\lambda_{\mathrm{k}}^n} \tag{A11}$$

Take a value α, $0 < \alpha < 1$, it gives

$$\dot{W}_1 \le -\alpha\|z\|^2 \tag{A12}$$

if

$$\|z\| \geq \delta_{\mathrm{z}} \tag{A13}$$

where $\delta_{\mathrm{z}} = \frac{2\lambda_{\max}(P_1)\gamma_2}{(1-\alpha)\lambda_{\mathrm{k}}^n}$ is a positive constant. As $\lambda_{\min}(P_1)\|z\|^2 \leq W_1(z) \leq \lambda_{\max}(P_1)\|z\|^2$, applying Corollary 5.3 of Theorem 5.1 of book Khalil (1996), one can conclude that if $\|z(0)\| \geq \delta_z$, there $\exists t_1, t_1 > 0$, such that

$$\|z(t)\| \leq \sqrt{\frac{\lambda_{\max}(P_1)}{\lambda_{\min}(P_1)}}\ \|z(0)\| e^{-\frac{\alpha}{(2\lambda_{\max}(P_1))}t}, \forall t < t_1 \tag{A14}$$

and

$$\|z(t)\| \leq \sqrt{\frac{\lambda_{\max}(P_1)}{\lambda_{\min}(P_1)}}\ \delta_{\mathrm{z}}\ ,\ \forall t \geq t_1 \tag{A15}$$

where

$$t_1 \leq \frac{2\lambda_{\max}(P_1)}{\alpha} \log\left(\frac{\|z\|}{\delta_z}\right) \tag{A16}$$

where t_1 is the time constant which definition can be found in reference Jiang et al. (2002).

As λ_{k} is always assumed to be larger than 1, we can observe from equation (A6) that

$$\|z\| \leq \|\tilde{x}_{\mathrm{e1}}\| \leq \lambda_{\mathrm{k}}^{n-1}\|z\| \tag{A17}$$

Thus the previous expressions can be written in terms of $\tilde{x}_{\mathrm{e1}}$ as

$$\|\tilde{x}_{\mathrm{e1}}(t)\| \leq \lambda_{\mathrm{k}}^{n-1}\sqrt{\frac{\lambda_{\max}(P_1)}{\lambda_{\min}(P_1)}}\|\tilde{x}_{\mathrm{e1}}(0)\| e^{-\frac{\alpha}{2\lambda_{\max}(P_1)}t},\ \forall t < t_1 \tag{A18}$$

$$\|\tilde{x}_{\mathrm{e1}}(t)\| \leq \lambda_{\mathrm{k}}^{n-1}\sqrt{\frac{\lambda_{\max}(P_1)}{\lambda_{\min}(P_1)}}\delta_{\mathrm{z}},\ \forall t \geq t_1 \tag{A19}$$

$$t_1 \leq \frac{2\lambda_{\max}(P_1)}{\alpha} \log\left(\frac{\|\tilde{x}_{\mathrm{e1}}(0)\|}{\delta_z}\right) \tag{A20}$$

Therefore, for a given positive constant δ, one can take λ_{k}, such that

$$\delta \geq \lambda_{\mathrm{k}}^{n-1}\sqrt{\frac{\lambda_{\max}(P_1)}{\lambda_{\min}(P_1)}}\delta_{\mathrm{z}} = \sqrt{\frac{\lambda_{\max}(P_1)}{\lambda_{\min}(P_1)}}\frac{2\lambda_{\max}(P_1)\gamma_2}{(1-\alpha)\lambda_{\mathrm{k}}} \tag{A21}$$

is satisfied. This will guarantee the exponential convergence of the observation error into

$$\|\tilde{x}_{\mathrm{e1}}\| \leq \delta,\ \forall t > t_1 \tag{A22}$$

In particular,

$$|\tilde{x}_i| \leq \frac{\delta}{\lambda_{\mathrm{k}}^{n+1-i}}\ ,\quad i = 2, \ldots, n+1,\ \forall t > t_1 \tag{A23}$$

To complete the proof, it is necessary to show that gain k_1 can be chosen such that sliding condition (A2) holds for all $t > 0$. It is obvious that

$$|\tilde{x}_2| = |z_2| \leq \|z\| \leq \sqrt{\frac{\lambda_{\max}(P_1)}{\lambda_{\min}(P_1)}}\|z(0)\| \leq \sqrt{\frac{\lambda_{\max}(P_1)}{\lambda_{\min}(P_1)}}\|\tilde{x}_{\mathrm{e1}}(0)\|, \forall t > 0 \tag{A24}$$

Therefore, for a given value of initial estimation error $\|\tilde{x}_{\mathrm{e1}}(0)\|$, the sliding condition will be fulfilled for all t if gain k_1 is chosen as

$$\boldsymbol{k_1 \geq \|\tilde{x}_{e1}(0)\|\sqrt{\frac{\lambda_{\max}(P_1)}{\lambda_{\min}(P_1)}}} \tag{A25}$$

Appendix B. Proof of Stability

The actual fractional-order sliding surface is written by

$$S_{\mathrm{FO}} = \sum_{i=1}^{n}[\rho_i\left(x_i - y_{\mathrm{d}}^{(i-1)}\right) + \mathrm{D}^{\alpha}\left(x_i - y_{\mathrm{d}}^{(i-1)}\right)] \tag{B1}$$

Hence, the estimation error of the sliding surface can be directly calculated as

$$\tilde{S}_{\mathrm{FO}} = S_{\mathrm{FO}} - \hat{S}_{\mathrm{FO}} = \sum_{i=1}^{n}(\rho_i\,\tilde{x}_i + \mathrm{D}^{\alpha}\tilde{x}_i) \tag{B2}$$

Construct a Lyapunov function as follows

$$V = \frac{1}{2}\hat{S}_{\mathrm{FO}}^2 \tag{B3}$$

The attractiveness of sliding surface is achieved if $\dot{V} < 0$ for all $\tilde{x} \notin \hat{S}_{\mathrm{FO}}$, that is, the control u needs to be designed to enforce $\hat{S}_{\mathrm{FO}}\dot{\hat{S}}_{\mathrm{FO}} < 0$ outside a prescribed manifold $\left|\hat{S}_{\mathrm{FO}}\right| < \varepsilon_{\mathrm{c}}$.

Differentiate estimated sliding surface (30) along SMSPO (18), use the reduced estimation error dynamics (A3), it yields

$$\dot{\hat{S}}_{\mathrm{FO}} = \hat{\Psi}(\cdot) + b_0 u + \frac{k_n}{k_1}\tilde{x}_2 - y_{\mathrm{d}}^{(n)} + \sum_{i=1}^{n-1}\left[\rho_i\left(\hat{x}_{i+1} - y_{\mathrm{d}}^{(i)} + \frac{k_i}{k_1}\tilde{x}_2\right) + \mathrm{D}^{\alpha}\left(\hat{x}_{i+1} - y_{\mathrm{d}}^{(i)} + \frac{k_i}{k_1}\tilde{x}_2\right)\right] \tag{B4}$$

Substitute control (32) into the above equation (B4), leads to

$$\dot{\hat{S}}_{\mathrm{FO}} = \sum_{i=1}^{n-1}\left[\rho_i\frac{k_i}{k_1}\tilde{x}_2 + \mathrm{D}^{\alpha}(\frac{k_i}{k_1}\tilde{x}_2)\right] - \zeta\hat{S}_{\mathrm{FO}} - \varphi\mathrm{sat}(\hat{S}_{\mathrm{FO}}, \varepsilon_{\mathrm{c}}) \tag{B5}$$

Consequently, the attractiveness of sliding surface can be derived as

$$\zeta \hat{S}_{\mathrm{FO}} + \varphi > \sum_{i=1}^{n-1} \left[\rho_i \frac{k_i}{k_1} |\tilde{x}_2| + \mathrm{D}^{\alpha}(\frac{k_i}{k_1} |\tilde{x}_2|) \right] \tag{B6}$$

which will be fulfilled with relationship (20) if

$$\zeta \hat{S}_{\mathrm{FO}} + \varphi > k_1 \sum_{i=1}^{n-1} \left[\rho_i \frac{k_i}{k_1} + \mathrm{D}^{\alpha}(\frac{k_i}{k_1}) \right] \tag{B7}$$

The above condition can be immediately satisfied if control gain φ is chosen as

$$\varphi > k_1 \sum_{i=1}^{n-1} \left[\rho_i \frac{k_i}{k_1} + \mathrm{D}^{\alpha}(\frac{k_i}{k_1}) \right] \tag{B8}$$

which, using gains (21), yields

$$\varphi > k_1 \sum_{i=1}^{n-1} \left[\rho_i C_n^{i-1} \lambda_{\mathrm{k}}^{i-1} + \mathrm{D}^{\alpha}(C_n^{i-1} \lambda_{\mathrm{k}}^{i-1}) \right] = k_1 \sum_{i=1}^{n-1} \rho_i C_n^{i-1} \lambda_{\mathrm{k}}^{i-1} \tag{B9}$$

This condition ensures the existence of a sliding mode on the boundary layer $\left|\hat{S}_{\mathrm{FO}}\right| \le \varepsilon_{\mathrm{c}}$. Now, one can easily calculate

$$\dot{\hat{S}}_{\mathrm{FO}} = \sum_{i=1}^{n-1} [\rho_i \tilde{x}_{i+1} + \mathrm{D}^{\alpha}(\tilde{x}_{i+1})] - \sum_{i=1}^{n-1} \left[\rho_i \frac{k_i}{k_1} \tilde{x}_2 + \mathrm{D}^{\alpha}(\rho_i \frac{k_i}{k_1} \tilde{x}_2) \right] + \tilde{\Psi}(\cdot) \tag{B10}$$

As $\hat{S}_{\mathrm{FO}} = S_{\mathrm{FO}} - \tilde{S}_{\mathrm{FO}}$, the actual S-dynamics of sliding surface can be obtained with dynamics (B5) as

$$\dot{S}_{\mathrm{FO}} + \left(\zeta + \frac{\varphi}{\varepsilon_{\mathrm{c}}}\right) S_{\mathrm{FO}} = \left(\zeta + \frac{\varphi}{\varepsilon_{\mathrm{c}}}\right) \sum_{i=1}^{n} [\rho_i \tilde{x}_i + \mathrm{D}^{\alpha}(\tilde{x}_i)] + \sum_{i=1}^{n-1} [\rho_i \tilde{x}_{i+1} + \mathrm{D}^{\alpha}(\tilde{x}_{i+1})] + \tilde{\Psi}(\cdot) \tag{B11}$$

It is definite that the driving term of S-dynamics is the sum of the estimation errors of states and the perturbation. The bounds of the sliding surface can be calculated by

$$\left|\hat{S}_{\mathrm{FO}}\right| \le \varepsilon_{\mathrm{c}} \Rightarrow \left|S_{\mathrm{FO}} - \tilde{S}_{\mathrm{FO}}\right| \le \varepsilon_{\mathrm{c}} \Rightarrow |S_{\mathrm{FO}}| \le \hat{S}_{\mathrm{FO}} + \varepsilon_{\mathrm{c}} \Rightarrow$$

$$|S_{\mathrm{FO}}| \le \left|\sum_{i=1}^{n} [\rho_i \tilde{x}_i + \mathrm{D}^{\alpha}(\tilde{x}_i)]\right| + \varepsilon_{\mathrm{c}} \le \frac{\delta}{\lambda_{\mathrm{k}}^{n+1}} \sum_{i=2}^{n} \rho_i \lambda_{\mathrm{k}}^{i} + \varepsilon_{\mathrm{c}}, \forall t > t_1. \tag{B12}$$

Based on bounds (B12), together with the polynomial gains $\rho_i = C_n^{i-1} \lambda_{\mathrm{c}}^{i-1}$, where $i = 1, \ldots, n-1$. The states tracking error satisfies the following relationship

$$\left| x^{(i)}(t) - x_{\mathrm{d}}^{(i)}(t) \right| \le (2\lambda_{\mathrm{c}})^i \frac{\varepsilon_{\mathrm{c}}}{\lambda_{\mathrm{c}}^n} + \frac{\delta}{\lambda_{\mathrm{k}}^{n+1}} \sum_{j=2}^{n} \left(\frac{\lambda_k}{\lambda_{\mathrm{c}}}\right)^j C_{n-1}^{j}, i = 0,1, \ldots, n-1 \tag{B13}$$

Acknowledgments

The authors gratefully acknowledge the support of National Natural Science Foundation of China (51477055, 51667010, 51777078).

References

Ahmed, J.; Salam, Z. (**2015**). An improved perturb and observe (P&O) maximum power point tracking (MPPT) algorithm for higher efficiency. *Applied Energy*, 150: 97-108.

Al-Dhaifallah M.; Nassef A. M.; Rezk H.; Nisar K. S. (**2018**). Optimal parameter design of fractional order control based INC-MPPT for PV system. *Solar Energy*, 159: 650-664.

Atangana, A. (**2016**). Derivative with two fractional orders: A new avenue of investigation toward revolution in fractional calculus. *European Physical Journal Plus*, 131(10): 373.

Abdel-Salam, M.; Kamel, R.; Khalaf, M.; Sayed, K. (**2015**) Analysis of overcurrent numerical-relays for protection of a stand-alone PV system. *IEEE Smart Grid Conference.*1-6.

Bounechba, H.; Bouzid, A.; Snani, H.; Lashab, A. (**2016**). Real time simulation of MPPT algorithms for PV energy system. *International Journal of Electrical Power & Energy Systems*, 83: 67-78.

Baghaee, H.R.; Mirsalim, M.; Gharehpetian, G.B. (**2016a**) Real-time verification of new controller to improve small/large-signal stability and fault ride-through capability of multi-DER microgrids. *IET Generation Transmission and Distribution*, 10(12): 3068-3084.

Baghaee, H.R.; Mirsalim, M.; Gharehpetian, G.B. (**2016b**) Power calculation using RBF neural networks to improve power sharing of hierarchical control scheme in multi-DER microgrids. *IEEE Journal of Emerging & Selected Topics in Power Electronics*, 4(4): 1217-1225.

Baghaee, H.R.; Mirsalim, M.; Gharehpetan, G.B; Talebi, H.A. (**2016c**) Nonlinear load sharing and voltage compensation of microgrids based on harmonic power-flow calculations using radial basis function neural networks. *IEEE Systems Journal*, DOI: 10.1109/JSYST.2016.2645165

Baghaee, H.R.; Mirsalim, M.; Gharehpetian, G.B.; Talebi, H.A. (**2018a**) Unbalanced harmonic power sharing and voltage compensation of microgrids using radial basis function neural network-based harmonic power-flow calculations for distributed and decentralised control structures. *IET Generation Transmission and Distribution*, 12(7): 1518-1530.

Baghaee, H.R.; Mirsalim, M.; Gharehpetian, G.B. (**2018b**) Performance improvement of multi-DER microgrid for small- and large-signal disturbances and nonlinear loads: Novel complementary control loop and fuzzy controller in a hierarchical droop-based control scheme. *IEEE Systems Journal*, 12(1): 444-451.

Chiu, C.S.; Ouyang, Y.L. (**2011**). Robust maximum power tracking control of uncertain photovoltaic systems: a unified T-S fuzzy model-based approach. I*EEE Transactions on Control Systems Technology*, 19(6): 1516-1526.

Dash, P.P.; Kazerani, M. (**2011**). Dynamic modelling and performance analysis of a grid-connected current-source inverter based photovoltaic system. *IEEE Transactions on Sustainable Energy*, 2(4): 443-450.

Delghavi, M.B.; Shoja-Majidabad, S.; Yazdani, A. (**2016**). Fractional-order sliding-mode control of islanded distributed energy resource systems. *IEEE Transactions on Sustainable Energy*, 7(4): 1482-1491.

Dhar, S.; Dash, P.K. (**2016**). A new backstepping finite time sliding mode control of grid connected PV system using multivariable dynamic VSC model. *International Journal of Electrical Power & Energy Systems*, 82: 314-330.

Dong, J.; Li, S.N.; Wu, S.J.; He, T.Y.; Yang, B.; Shu, H.C.; Yu, J.L. (**2017**) Nonlinear observer based robust passive control of DFIG for power system stability enhancement via energy reshaping, *Energies*, vol. 10, 1082; doi:10.3390/en10081082.

Ebrahimkhani, S. (**2016**). Robust fractional order sliding mode control of doubly-fed induction generator (DFIG)-based wind turbines. *ISA Transactions*, 63: 343-354.

Elobaid, L.M.; Abdelsalam, A.K.; Zakzouk, E.E. (**2015**). Artificial neural network-based photovoltaic maximum power point tracking techniques: a survey. *IET Renewable Power Generation*, 9(8): 1043-1063.

Farhat, M.; Barambones, O.; Sbita, L. (**2017**). A new maximum power point method based on a sliding mode approach for solar energy harvesting. *Applied Energy*, 185(2): 1185-1198.

Guisser, M.; El-Jouni, A.; Abdelmounim, E.H. (**2014**). Robust sliding mode MPPT controller based on high gain observer of a photovoltaic water pumping system. *International Review of Automatic Control*, 7(2): 225-232.

Guerrero, J.M.; Vasquez, J.C.; Matas, J.; Vicuna, L.G.; Castilla, M. (**2010**) Hierarchical control of droop-controlled AC and DC microgrids-A general approach toward standardization. *IEEE Transactions on Industrial Electronics*, 58(1): 158-172.

Guerrero, J.M.; Chandorkar, M.; Lee, T.L.; Loh, P.C. (**2013**) Advanced control architectures for intelligent microgrids-Part I: Decentralized and hierarchical control. *IEEE Transactions on Industrial Electronics*, 60(4): 1254-1262.

Jiang, L.; Wu, Q.H.; Wen, J.Y. (**2002**). Nonlinear adaptive control via sliding-mode state and perturbation observer. *IEE Proceedings of Control Theory Applications*, 149: 269-277.

Khalil, H. K. 1996, *Nonlinear systems* (2nd edn). Prentice Hall London.

Kadri, R.; Gaubert, J.P.; Champenois, G. (**2011**). An improved maximum power point tracking for photovoltaic grid-connected inverter based on voltage-oriented control. *IEEE Transactions on Industrial Electronics*, 58(1): 66-75.

Kandemir, E.; Cetin, N.S.; Borekci, S. (**2017**). A comprehensive overview of maximum power extraction methods for PV systems. *Renewable and Sustainable Energy Reviews*, 78: 93-112.

Kchaou, A.; Naamane, A.; Koubaa, Y.; M'sirdi, N. (**2017**). Second order sliding mode-based MPPT control for photovoltaic applications. *Solar Energy*, 155: 758-769.

Kim, D.J.; Kim, B.; Ko, H.S.; Jang, M.S.; Ryu, K.S. (**2017**). A novel supervisory control algorithm to improve the performance of a real-time PV power-hardware-in-loop simulator with non-rtds. *Energies*, 10(10): 1651.

Kotsopoulos, A.; Duarte, J.L.; Hendrix, M.A.M. (**2001**). A predictive control scheme for DC voltage and AC current in grid-connected photovoltaic inverters with minimum DC link capacitance. *IEEE Conference of Industrial Electronics Society*, 1994-1999, vol.3. Denver, CO, USA,

Kharb, R.K.; Shimi, S.L.; Chatterji, S.; Ansari, M.F. (**2014**). Modeling of solar PV module and maximum power point tracking using ANFIS. *Renewable and Sustainable Energy Reviews*, 33(5): 602-612.

Lai, C.S., Mcculloch, M.D., Yan, J. (**2017**). Levelized cost of electricity for solar photovoltaic and electrical energy storage. *Applied Energy*, 190: 191-203.

Lalili, D.; Mellit, A.; Lourci, N.; Medjahed, B.; Berkouk, E.M. (**2011**). Input output feedback linearization control and variable step size MPPT algorithm of a grid-connected photovoltaic inverter. *Renewable Energy*, 36: 3282-3291.

Lalili, D.; Mellit, A.; Lourci, N.; Medjahed, B.; Boubakir, C. (**2013**). State feedback control and variable step size MPPT algorithm of three-level grid-connected photovoltaic inverter. *Solar Energy*, 98: 561-571.

Lauria, D.; Coppola, M. (**2014**). Design and control of an advanced PV inverter. *Solar Energy*, 110: 533-542.

Li, G.; Wang, H.A. (**2009**). A novel stand-alone PV generation system based on variable step size INC MPPT and SVPWM control. *IEEE 6th International Power Electronics and Motion Control Conference*, 2155-2160, Wuhan, China.

Liu, X.; Zhang, S.; Bae J. (**2017**). The nexus of renewable energy-agriculture-environment in BRICS. *Applied Energy*, 204: 489-496.

Liao, S.W.; Yao, W.; Han, X.N.; Wen, J.Y.; Cheng, S.J. (**2017**). Chronological operation simulation framework for regional power system under high penetration of renewable energy using meteorological data. *Applied Energy*, 203: 816-828.

Liu, J.; Wen, J.Y.; Yao, W.; Long, Y. (**2016**). Solution to short-term frequency response of wind farms by using energy storage systems. *IET Renewable Power Generation*, 10(5): 669-678.

Mahmud, M.A.; Pota, H.R.; Hossain, M.J., Roy, N.K. (**2013**). Robust partial feedback linearizing stabilization scheme for three-phase grid-connected photovoltaic systems. *IEEE Journal of Photovoltaics*, 4(1): 423-431.

Matignon, D. (**1998**). Stability properties for generalized fractional differential systems, *Esaim Proceedings*, 5(5): 145-158.

Mayyas, A.R.; Kumar, S.; Pisu, P.; Rios, J.; Jethani, P. (**2017**). Model-based design validation for advanced energy management strategies for electrified hybrid power trains using innovative vehicle hardware in the loop (VHIL) approach. *Applied Energy*, 204: 287-302.

Mi, Y.; Fu, Y.; Li, D.D.; Wang, C.S.; Loh, P.C.; Wang, P. (**2016**). The sliding mode load frequency control for hybrid power system based on disturbance observer. *International Journal of Electric Power and Energy Systems*, 74: 446-452.

Mirhosseini, M.; Pou, J.; Agelidis, V.G. (**2015**). Single- and Two-stage inverter-based grid-connected photovoltaic power plants with ride-through capability under grid faults. *IEEE Transactions on Sustainable Energy*, 6(3): 1150-1159.

Mojallal, A.; Lotfifard, S. (**2017**). Enhancement of grid connected PV arrays fault ride through and post fault recovery performance. I*EEE Transactions on Smart Grid*. DOI: 10.1109/TSG.2017.2748023.

Mojallizadeh, M.R.; Badamchizadeh, M.; Khanmohammadi, S.; Sabahi, M. (**2016**). Designing a new robust sliding mode controller for maximum power point tracking of photovoltaic cells. *Solar Energy*, 132: 538-546.

Podlubny, I. Fractional differential equations, Academic Press, New York, 1999.

Rahim, N.A.; Selvaraj, J.; Krismadinata, C.C. (**2007**). Hysteresis current control and sensorless MPPT for grid-connected photovoltaic systems. *IEEE International Symposium on Industrial Electronics*, 572-577.

Rezkallah, M.; Hamadi, A.; Chandra, A.; Singh, B. (**2015**). Real-time HIL implementation of sliding mode control for standalone system based on PV array without using dumpload. *IEEE Transactions on Sustainable Energy*, 6(4): 1389-1398.

Shen, Y.; Yao, W.; Wen, J.Y.; He, H.B. (**2017**). Adaptive wide-area power oscillation damper design for photovoltaic plant considering delay compensation. *IET Generation, Transmission and Distribution*, 11(18), 4511-4519.

Shen, Y.; Yao, W.; Wen, J.Y.; He, H.B.; Chen, W.B. (**2018**). Adaptive supplementary damping control of VSC-HVDC for interarea oscillation using GrHDP. *IEEE Transactions on Power Systems*, **33**(2), 1777-1789.

Sahan, B.; Vergara, A.N.; Henze, N.; Engler, A.; Zacharias, P. (**2008**). A single-stage PV module integrated converter based on a low-power current-source inverter. *IEEE Transactions on Industrial Electronics*, 55(7): 2602-2609.

Tang, R. L.; Wu, Z.; Fang, Y. J. (**2017**). Configuration of marine photovoltaic system and its MPPT using model predictive control. *Solar Energy*, 158: 995-1005.

Tang, Y.; Zhang, X.; Zhang, D.; Zhao, G.; Guan, X. (**2013**). Fractional order sliding mode controller design for antilock braking systems. *Neurocomputing*, 111(6): 122-130.

Wang, H.; Jin, X.; Zhao, H., Yue Y.J. (**2017**). MPPT control method of PV system based on active disturbance rejection control. *IEEE International Conference on Mechatronics and Automation*, 337-341, Takamatsu, Japan.

Wang, Y.; Ren, B. (**2018**). Fault ride-through enhancement for grid-tied PV systems with robust control. *IEEE Transactions on Industrial Electronics*, 65(3): 2302-2312.

Yang, B.; Jiang, L.; Wang, L.; Yao, W.; Wu, Q.H. (**2016a)**. Nonlinear maximum power point tracking control and modal analysis of DFIG based wind turbine. *International Journal of Electrical Power & Energy Systems*, 74: 429-436.

Yang, B.; Yu, T.; Shu, H. C.; Dong, J.; Jiang, L. (**2018a**). Robust sliding-mode control of wind energy conversion systems for optimal power extraction via nonlinear perturbation observers. *Applied Energy*, 210: 711-723.

Yang, B.; Sang, Y.Y.; Shi, K.; Yao, W.; Jiang, L.; Yu, T. (**2016b**). Design and real-time implementation of perturbation observer based sliding-mode control for VSC-HVDC systems. *Control Engineering Practice*, 56: 13-26

Yang, B.; Hu, Y.L.; Huang, H.Y.; Shu, H.C.; Yu, T.; Jiang, L. (**2017a**). Perturbation estimation based robust state feedback control for grid connected DFIG wind energy conversion system. *International Journal of Hydrogen Energy*, 42(33): 20994-21005.

Yang, B.; Zhang, X.S.; Yu, T.; Shu, H.C.; Fang, Z.H. (**2017b**). Grouped grey wolf optimizer for maximum power point tracking of doubly-fed induction generator based wind turbine. *Energy Conversion and Management*, 133: 427-443.

Yang, B.; Yu, T.; Shu, H.C.; Zhang, Y.M.; Chen, J.; Sang, Y.Y.; Jiang, L. (**2018b**). Passivity-based sliding-mode control design for optimal power extraction of a PMSG based variable speed wind turbine, *Renewable Energy*, 119: 577-589.

Yang, B.; Yu, T.; Shu, H.C.; Zhu, D.N.; An, N.; Sang, Y.Y.; Jiang, L. **(2018c)** Energy reshaping based passive fractional-order PID control design of a grid-connected photovoltaic inverter for optimal power extraction using grouped grey wolf optimizer, *Solar Energy*, 170: 31-46.

Yang, B.; Yu, T.; Shu, H.C.; Zhu, D.N.; Zeng, F.; Sang, Y.Y.; Jiang, L. **(2018d)** Perturbation observer based fractional-order PID control of photovoltaics inverters for solar energy harvesting via Yin-Yang-Pair optimization, *Energy Conversion and Management*. 171: 170-187.

Yang, B.; Jiang, L.; Yu, T.; Shu, H.C.; Zhang, C.K.; Yao, W.; Wu, Q.H. (**2018e**) Passive control design for multi-terminal VSC-HVDC systems via energy shaping, *International Journal of Electrical Power and Energy Systems*. 98: 496-508.

Yuan, Z.; Li, S.E.; Shao, B.; Wang, B. (**2016**). State-space model with non-integer order derivatives for lithium-ion battery. *Applied Energy*, 161: 330-336.

Yao, W.; Jiang, L.; Wen, J.Y.; Wu, Q.H.; Cheng, S.J. (**2015**). Wide-area damping controller for power system inter-area oscillations: a networked predictive control approach. *IEEE Transactions on Control Systems Technology*, 23(1), 27-36.

Zhang, B.; Pi, Y.; Luo, Y. (**2012**). Fractional order sliding-mode control based on parameters auto-tuning for velocity control of permanent magnet synchronous motor. *ISA Transactions*, 51(5): 649-656.